Large-amplitude high-frequency waves at Earth's magnetopause

D. B. Graham [1], A. Vaivads [1], Yu. V. Khotyaintsev [1], M. André [1], O. Le Contel [2], D. M. Malaspina [3], P.-A. Lindqvist [4], F. D. Wilder [3], R. E. Ergun [3], D. J. Gershman [5,6], B. L. Giles [5], W. Magnes [7], C. T. Russell [8], J. L. Burch [9], R. B. Torbert [10]

[1]Swedish Institute of Space Physics, Uppsala, Sweden.
[2]Laboratoire de Physique des Plasmas (LPP), UMR7648, CNRS, Ecole Polytechnique, UPMC Univ Paris 06, Univ. Paris-Sud, Observatoire de Paris, Paris, France
[3]Laboratory of Atmospheric and Space Physics, University of Colorado, Boulder, CO, USA.
[4]Space and Plasma Physics, School of Electrical Engineering, KTH Royal Institute of Technology, Stockholm, Sweden.
[5]NASA Goddard Space Flight Center, Greenbelt, MD, USA.
[6]Department of Astronomy, University of Maryland, College Park, MD, USA.
[7]Space Research Institute, Austrian Academy of Sciences, Graz, Austria.
[8]Department of Earth and Space Sciences, University of California, Los Angeles, CA, USA.
[9]Southwest Research Institute, San Antonio, TX, USA.
[10]Space Science Center, University of New Hampshire, Durham, NH, USA.

Key Points:

- 1: Large-amplitude upper hybrid and Langmuir waves frequently occur at Earth's magnetopause, reaching a maximum amplitude of 1 V m^{-1}.
- 2: The waves are quasi-electrostatic but electromagnetic properties are observed.
- 3: The upper hybrid and Langmuir wave properties are consistent with predictions from linear kinetic theory.

Corresponding author: D. B. Graham, dgraham@irfu.se

Abstract

Large-amplitude waves near the electron plasma frequency are found by the Magnetospheric Multiscale (MMS) mission near Earth's magnetopause. The waves are identified as Langmuir and upper hybrid (UH) waves, with wave vectors either close to parallel or close to perpendicular to the background magnetic field. The waves are found all along the magnetopause equatorial plane, including both flanks and close to the subsolar point. The waves reach very large amplitudes, up to $1\,\mathrm{V\,m^{-1}}$, and are thus amongst the most intense electric fields observed at Earth's magnetopause. In the magnetosphere and on the magnetospheric side of the magnetopause the waves are predominantly upper hybrid (UH) waves although Langmuir waves are also found. When the plasma is very weakly magnetized only Langmuir waves are likely to be found. Both Langmuir and UH waves are shown to have electromagnetic components, which are consistent with predictions from kinetic wave theory. These results show that the magnetopause and magnetosphere are often unstable to intense wave activity near the electron plasma frequency. These waves provide a possible source of radio emission at the magnetopause.

1 Introduction

Electron plasma frequency waves, specifically Langmuir and upper hybrid (UH) waves, are commonly observed in plasmas. Langmuir waves are narrowband electrostatic waves observed near the local electron plasma frequency f_{pe}. Upper hybrid waves are quasi-electrostatic waves, which have frequencies close to the UH frequency f_{uh}. It is well known that Langmuir and UH waves both lie on the same dispersion surface [*Stix*, 1962; *André*, 1985], with Langmuir waves occurring for wave vectors closely aligned with the background magnetic field $\mathbf{B}_0$, while UH waves have wave vectors close to perpendicular to $\mathbf{B}_0$.

Langmuir waves are commonly observed in the solar wind, planetary foreshocks, ionosphere auroral regions, and radiation belts. Langmuir waves are of particular importance because they are sources of radio emission at the electron plasma frequency f_{pe} and its harmonics, via the plasma emission mechanism. The plasma emission mechanism involves several steps: electron beams develop, the electron beams then generate Langmuir waves, and these Langmuir waves are converted to radio waves via linear and/or nonlinear processes. Various mechanisms have been proposed for the conversion of Langmuir waves to radio waves, including linear mode conversion [*Field*, 1956; *Yin et al.*, 1998; *Kim* *et al.*, 2007], electromagnetic decay [*Cairns*, 1987], electrostatic decay and coalescence [*Cairns*, 1987], and antenna mechanisms [*Malaspina et al.*, 2010]. There remains debate over which processes occur and when.

Large-amplitude UH waves have been observed at Earth's plasmapause [*Kurth et al.*, 1979]. At the plasmapause UH waves (and the closely related Bernstein waves) are commonly observed at density gradients, and are thought to be the source of nonthermal continuum radiation [*Kurth*, 1982] observed in Earth's magnetosphere [*Gurnett*, 1975]. UH waves can generate radio waves via linear mode conversion [*Oya*, 1971], nonlinear three-wave processes [*Melrose*, 1981], or both. Although the primary source of nonthermal continuum radiation was found to be at the plasmapause, some observations suggest that the magnetopause may also be a source of radio wave emission [*Kurth et al.*, 1981; *Jones*, 1987]. Several studies have found that Langmuir and/or UH waves occur at the magnetopause [*Gurnett et al.*, 1979; *Anderson et al.*, 1982]. However, there is currently a lack of detailed studies on the properties of the waves near f_{pe} at Earth's magnetopause.

Langmuir waves are well known to be generated by fast electron beams via the bump-on-tail (or beam-plasma) instability [*Scarf et al.*, 1971]. These beams form in the solar wind (from the Sun or CME shocks) [*Lin et al.*, 1981; *Ergun et al.*, 1998] and at Earth's quasi-perpendicular foreshock [*Fitzenreiter et al.*, 1990]. Electron beams have also been observed at Earth's magnetopause associated with magnetic reconnection [*Graham et al.*, 2016; *Wilder et al.*, 2016], potentially generating Langmuir or beam-mode waves. Upper hybrid (UH) waves can be generated by electron distributions with $df/dv_{\perp} > 0$ [*Winglee and Dulk*, 1986], such as ring, shell, or loss-cone distributions [*Tataronis and Crawford*, 1970; *Kurth et al.*, 1980; *Wong et al.*, 1988]. These distributions could occur near the magnetopause. Such electron distributions can also be produced by magnetic reconnection at the magnetopause [*Graham et al.*, 2016]. Thus, magnetic reconnection at Earth's magnetopause provides a source of Langmuir and UH waves. Previous observations show that Langmuir and UH waves can develop in magnetic reconnection separatrices [*Farrell et al.*, 2002; *Farrell et al.*, 2003; *Khotyaintsev et al.*, 2004; *Vaivads et al.*, 2004; *Retinò et al.*, 2006; *Viberg et al.*, 2013] and close to the electron diffusion region [*Graham et al.*, 2017].

At present there is a lack of detailed investigations of the properties of Langmuir and UH waves at Earth's magnetopause. In this paper we investigate the properties of large-amplitude waves near the electron plasma frequency observed by the Magnetospheric Multiscale (MMS) mission [*Burch et al.*, 2016]. The outline of this paper is as follows: In section 2 we present the wave properties predicted for the dispersion surfaces near the electron plasma frequency f_{pe} using kinetic theory. In section 3 we provide an overview of the MMS data used. Sections 4, 5, and 6 present the observations, discussion, and conclusions of this paper, respectively.

2 Theory

In this section we briefly review the linear kinetic theory of the waves near the electron plasma frequency f_{pe}. For a single Maxwellian electron distribution three dispersion surfaces are predicted near f_{pe} (the magnetoionic modes in cold plasma theory) [*Stix*, 1962]. In Figures 1–3 we plot these three dispersion surfaces using the WHAMP (Waves in Homogeneous, Anisotropic, Multicomponent Plasmas) dispersion equation solver [*Rönnmark*, 1982]. We use a single electron Maxwellian distribution and nominal magnetospheric conditions: Electron density $n_e = 0.5\,\mathrm{cm}^{-3}$, electron temperature $T_e = 200\,\mathrm{eV}$, and magnetic field strength $B_0 = 50\,\mathrm{nT}$. The ratio of f_{pe} to electron cyclotron frequency f_{ce} is $f_{pe}/f_{ce} = 4.5$ for these conditions. For all events in this paper $f_{pe} > f_{ce}$ so only the Langmuir and L-mode dispersion relations cross for parallel propagation [*André*, 1985]. (The whistler mode below f_{ce} does not connect with the Langmuir wave and is not considered in detail here.)

Figure 1 shows the Langmuir/Z mode and UH dispersion surface, Figure 2 shows the left-hand electromagnetic-ordinary (L-O) mode dispersion surface, and Figure 3 shows the right-hand electromagnetic-extraordinary (R-X) mode dispersion surface [*André*, 1985]. For each of these surfaces we plot the fraction of perpendicular electric field power to total electric field power $F_E = E_\perp^2/E^2$ (panels a), fraction of perpendicular magnetic field power to total magnetic field power $F_B = B_\perp^2/B^2$ (panels b), $c|\mathbf{B}|/|\mathbf{E}|$ (panels c), fraction of parallel to total Poynting flux $S_\parallel/S$ (panels d), ellipticity of the electric field $\mathbf{E}$ with respect to the background magnetic field $\mathbf{B}_0$ (panels e), and ellipticity of the fluctuating magnetic field $\mathbf{B}$ with respect to $\mathbf{B}_0$ (panels f). We have plotted these properties because, assuming magnetic field $\mathbf{B}$ fluctuations can be seen, all these parameters are straightforward to calculate from observations without *a priori* knowledge of the wave vector $\mathbf{k}$ direction. Computing these parameters enables the mode to be identified in observations.

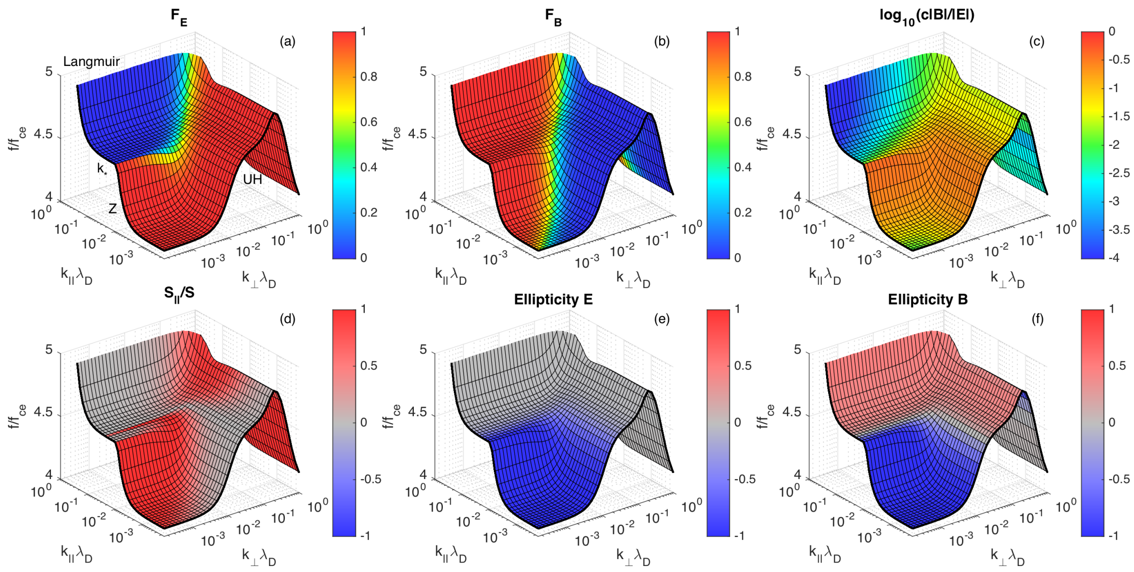

Figure 1. Langmuir/Z-mode and upper hybrid dispersion surface. (a) F_E. (b) F_B. (c) $c|\mathbf{B}|/|\mathbf{E}|$. (d) $S_{\|}/S$. (e) Ellipticity of **E**. (f) Ellipticity of **B**. The dispersion surface is computed from a single electron Maxwellian distribution for parameters $n_e = 0.5\,\mathrm{cm}^{-3}$, $T_e = 200\,\mathrm{eV}$, and $B_0 = 50\,\mathrm{nT}$. The wave numbers k are normalized to the Debye length λ_D.

The Langmuir/Z-mode and UH dispersion surface consists of the generalized Langmuir/Z-mode wave for $\mathbf{k}$ closely aligned with $\mathbf{B}_0$. For large wave numbers k, the wave is approximately electrostatic, while at low k the wave is electromagnetic and left-hand circularly polarized. The mode switches from Langmuir-like to Z-mode-like at wave number $k_* \lambda_D = v_e/(c\sqrt{2})(1 + f_{pe}/f_{ce})^{-1/2}$, which also corresponds to the window where mode conversion between the Langmuir/Z-mode and O mode occurs [*Ellis*, 1956; *Yoon et al.*, 1998]. Here, $v_e = \sqrt{2k_B T_e/m_e}$ is the electron thermal speed. The cutoff of the Z-mode occurs at frequency $f = (\sqrt{f_{ce}^2 + 4f_{pe}^2} - f_{ce})/2$ as $k \to 0$. For $\mathbf{k}$ approximately perpendicular to $\mathbf{B}_0$ the dispersion relation is the generalized UH wave. At low k the wave is the left-hand polarized Z-mode (sometimes called the slow extraordinary mode). For moderate values of k the mode follows the UH dispersion relation and crosses the UH resonance frequency $f_{uh} = \sqrt{f_{pe}^2 + f_{ce}^2}$ for finite T_e due to thermal effects. For large k the frequency f peaks and as k is increased f decreases to the nearest harmonic of f_{ce}. Here the mode is Bernstein-like, and only develops in kinetic plasma theory. In this paper we will investigate large-amplitude non-thermal waves near f_{pe}, so the observed waveforms will likely lie on this dispersion surface.

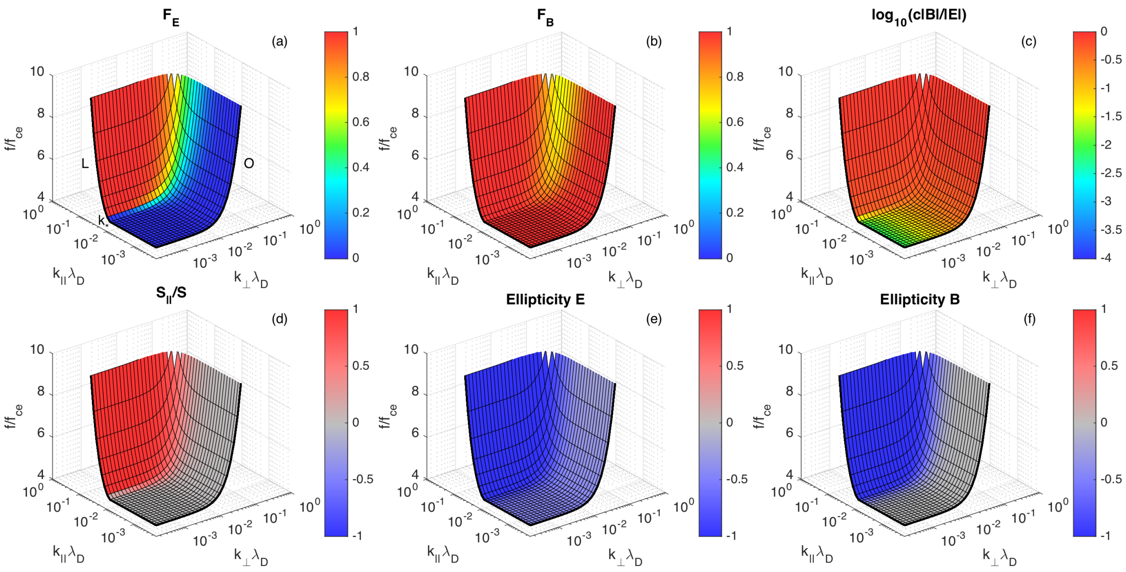

Figure 2. L-O mode dispersion surface. (a) F_E. (b) F_B. (c) $c|\mathbf{B}|/|\mathbf{E}|$. (d) $S_{\|}/S$. (e) Ellipticity of $\mathbf{E}$. (f) Ellipticity of $\mathbf{B}$.

Figure 2 shows the L-O dispersion surface. For $\mathbf{k}$ along $\mathbf{B}_0$ and small k the wave is Langmuir like until k_*, where the mode connects with the electromagnetic left-hand polarized L mode. For $\mathbf{k}$ approximately perpendicular to $\mathbf{B}_0$ the dispersion surface corresponds to the electromagnetic O mode. This surface has a cutoff at $f = f_{pe}$. The uppermost dispersion surface (Figure 3) shows the electromagnetic right-hand polarized R mode wave for $\mathbf{k}$ along $\mathbf{B}_0$. For $\mathbf{k}$ approximately perpendicular to $\mathbf{B}_0$ the X mode wave is found. This dispersion surface has a cutoff of $f = (\sqrt{f_{ce}^2 + 4f_{pe}^2} + f_{ce})/2$.

Below we summarize the electromagnetic properties of the dispersion surfaces based on the parameters plotted in Figures 1–3:

(1) From each panel (a) we see that F_E changes significantly between dispersion surfaces and depends strongly on the direction of $\mathbf{k}$. For the Langmuir wave and O mode wave $F_E \sim 0$, corresponding to $\mathbf{E}$ aligned with $\mathbf{B}_0$. The remaining modes are characterized by $F_E \sim 1$, meaning $\mathbf{E}$ is approximately perpendicular to $\mathbf{B}_0$. Note that intermediate values of F_E are only found for oblique $\mathbf{k}$ and $F_E \sim 0$ does not occur on the R-X surface.

(2) Panels (b) show F_B for each dispersion surface. For $\mathbf{k}_{\|} \gg \mathbf{k}_{\perp}$, $F_B \sim 1$ for all dispersion surfaces; for $\mathbf{k}_{\perp} \gg \mathbf{k}_{\|}$, $F_B \sim 0$ for the Langmuir/UH and R-X surfaces, while $F_B \sim 1$ for the L-O surface. Note that F_B remains large for all $\mathbf{k}$ on the L-O surface.

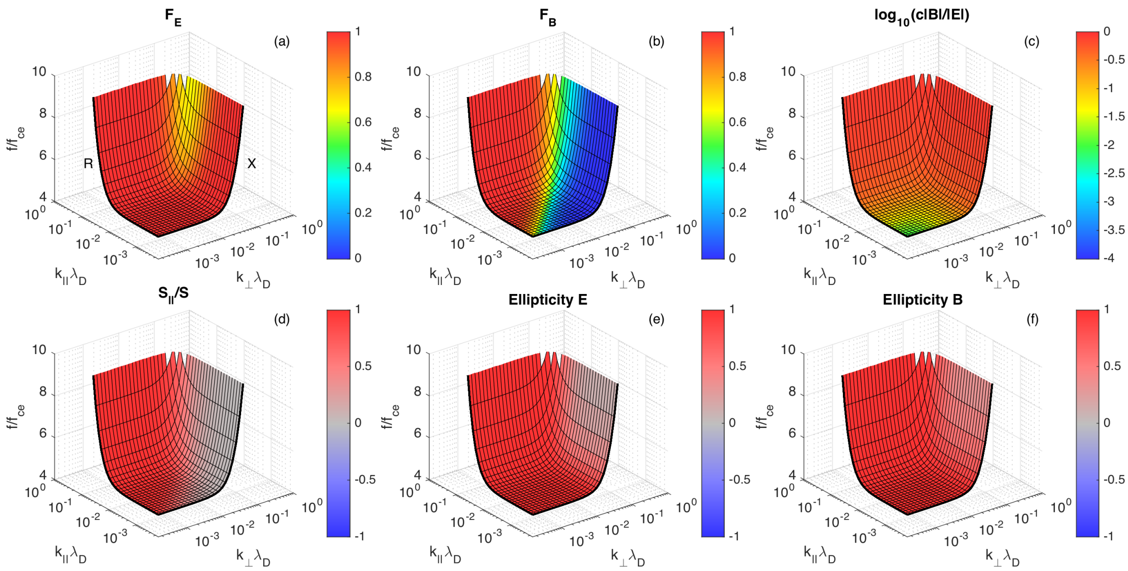

Figure 3. R-X mode dispersion surface. (a) F_E. (b) F_B. (c) $c|\mathbf{B}|/|\mathbf{E}|$. (d) $S_{\|}/S$. (e) Ellipticity of **E**. (f) Ellipticity of **B**.

(3) Panels (c) show $c|\mathbf{B}|/|\mathbf{E}|$, where $c|\mathbf{B}|/|\mathbf{E}| \rightarrow 0$ corresponds to purely electrostatic waves, while $c|\mathbf{B}|/|\mathbf{E}| = 1$ indicates freely propagating electromagnetic waves. Both the L-O and R-X waves approach $c|\mathbf{B}|/|\mathbf{E}| = 1$ at large k. In contrast, for Langmuir and UH waves $c|\mathbf{B}|/|\mathbf{E}|$ is maximal for small k, close to where the transition from the Z-mode to Langmuir and UH waves occurs. For UH waves $c|\mathbf{B}|/|\mathbf{E}|$ remains finite over a range of k, but decreases in the Bernstein-like portion of the mode at large $k_\perp$. For Langmuir waves $c|\mathbf{B}|/|\mathbf{E}|$ is negligible for $k_\perp = 0$, although finite $c|\mathbf{B}|/|\mathbf{E}|$ is predicted for Langmuir waves with slightly oblique **k**.

(4) Panels (d) show the ratio $S_{\|}/S$ of the parallel to total Poynting flux. For the quasi-electrostatic Langmuir and UH waves $S_{\|}/S = 0$, while for large $k_\perp$, $S_{\|}/S = 1$ for the Bernstein-like part of the dispersion surface in Figure 1. For the electromagnetic waves aligned with $\mathbf{B}_0$, $S_{\|}/S = 1$, while $S_{\|}/S = 0$ for the O and X modes with $k_\perp \gg k_{\|}$.

(5) Panels (e) show the ellipticity of **E** computed from the components of **E** perpendicular to $\mathbf{B}_0$. For Langmuir and UH waves the ellipticity is ≈ 0 (linear polarization). At low k (Z mode) the ellipticity is -1, corresponding to left-hand circular polarization. The L-O surface is characterized by left-hand polarization, and the R-X surface has right-hand polarization, with the X mode having linear polarization for large $k_\perp$.

(6) Panels (f) show the ellipticity of **B**. In general, the ellipticity of **B** closely resembles the ellipticity of **E**. The only major difference between the two is found on the Langmuir/UH dispersion surface. For Langmuir and UH waves right-hand polarized **B** is predicted, while for **E** the ellipticity is approximately 0 (linear polarization) for the same **k**. Note that for UH waves $F_B \approx 0$, so **B** is approximately parallel to $\mathbf{B}_0$. For the parameters used in Figure 1 the polarization of **B** is elliptical. Model calculations (not shown) show that the ellipticity of **B** depends on f_{pe}/f_{ce}, with the ellipticity of **B** approaching 1 for $k_\parallel \gg k_\perp$ as f_{pe}/f_{ce} approaches 1. For large f_{pe}/f_{ce} the ellipticity of **B** approaches 0 at moderate **k**.

We note that these plots show that the Langmuir wave, typically assumed to be a purely electrostatic wave, can have an electromagnetic component. Specifically, for slightly oblique **k** there is a region of the dispersion surface where $F_E \sim 0$, $F_B \sim 1$, right-hand polarization of **B**, and non-negligible $c|\mathbf{B}/|\mathbf{E}|$. Therefore, in theory, it is possible to measure the electromagnetic signatures associated with Langmuir waves.

In addition to these modes, electron Bernstein waves are predicted in a kinetic plasma [*Bernstein*, 1958]. These waves are found for wave vectors **k** close to perpendicular to $\mathbf{B}_0$. For $f < f_{pe}$ the Bernstein modes are bounded by harmonics of f_{ce}, while for $f > f_{pe}$ the waves are found just above harmonics of f_{ce} [*André*, 1985]. When electron beams are present the beam mode wave $\omega \approx k v_b$ can be excited, where v_b is the electron beam speed, which for fast electron beams has a dispersion relation characterized by a roughly linear increase in ω with k, until ω_{pe} is approached, at which point ω only increases slowly with k.

Finally, we note that a single Maxwellian distribution is highly idealized and is unlikely to be observed at Earth's magnetopause (or in any collisionless plasma), and more complex electron distributions will modify the linear dispersion relations of Langmuir and UH waves. However, the properties shown in Figure 1 are generally only weakly modified, so they can be compared with observations. Appendix A: shows an example of the Langmuir and UH wave properties for an electron distribution with distinct hot and cold components.

3 MMS Data

We use data from the MMS spacecraft [*Burch et al.*, 2016]. The four MMS spacecraft orbit Earth in a tetrahedral configuration. In this paper we investigate data from phases 1a and 1b of the MMS mission; the two magnetopause science phases. Over these phases the inter-spacecraft separations ranged from $\sim$ 100 km down to $\sim$ 5 km. We use three-dimensional electric field data from electric field double probes (EDP) [*Lindqvist et al.*, 2016; *Ergun et al.*, 2016], magnetic field data from fluxgate magnetometer (FGM) [*Russell et al.*, 2016] and search-coil magnetometer (SCM) [*Le Contel et al.*, 2016], and particle data from fast plasma investigation (FPI) [*Pollock et al.*, 2016]. All data presented in this paper are from high-resolution burst mode intervals. To analyze the waves at the plasma frequency we use the high-frequency AC coupled electric field (termed hmfe data). These data typically have a sampling rate of 65.536 kHz; a small fraction of the data have a sampling rate of 131.072 kHz. For the typical sampling rate we expect waves at the local electron plasma frequency $f_{pe} \lesssim 32$ kHz to be resolved for electron number densities $n_e \lesssim 13\,\mathrm{cm}^{-3}$. These hmfe data are measured intermittently over burst mode intervals with median durations of 2 s. The high-frequency SCM data are sampled at 16.384 kHz over the same intervals as the hmfe data. Thus, for SCM data $n_e \lesssim 0.8\,\mathrm{cm}^{-3}$ is required to resolve $f_{pe} \lesssim 8$ kHz, restricting the investigation of the electromagnetic properties of the waves to the magnetosphere and magnetospheric side of the magnetopause, where densities are low.

In this paper we define a *wave event* as an interval of hmfe data (median duration of 2 s) with large-amplitude waves near f_{pe}. Thus, a single burst mode interval (composed of multiple hmfe data intervals) can contain multiple wave events. To find wave events we use a semi-automated routine and the following criteria:

(1) Burst mode $\mathbf{B}_0$ data from FGM and particle (specifically electron) moments are available, and f_{pe} calculated from the median n_e over the wave event time interval is below the Nyquist frequency of the electric field data.

(2) The maximum wave amplitude high-pass filtered above $f_{pe}/1.5$ is over $20\,\mathrm{mV\,m}^{-1}$ (our *ad hoc* definition of large amplitude).

(3) Waves with very broadband spectra, such as fast moving electrostatic solitary waves or broadband electrostatic turbulence, which can lead to large fields near f_{pe} but no well defined spectral peak near f_{pe} have been removed from the dataset.

Despite criterion (2) being seemingly strict we still identify a total of ~9000 wave events from the four spacecraft. The number of wave events are comparable on each spacecraft. This number of wave events corresponds to about 2.3% of the hmfe intervals satisfying criterion (1). This percentage will increase for lower threshold electric field strengths. Thus, we can therefore conclude that large-amplitude plasma frequency waves are common at the magnetopause.

The use of MMS burst mode data introduces a number of selection biases, which are important when considering the statistical results presented in the next section. Of particular importance are:

(1) The burst mode intervals are selected by the Scientist In The Loop (SITL) during the magnetopause Regions of Interest (ROIs) lasting about 12 hours. As a result almost all wave events are found at distances between $9R_E$ and $12R_E$ from Earth, where R_E is Earth's radius. Since MMS is focused on observing magnetic reconnection, the burst mode intervals telemetered to Earth were selected based on how interesting they appear (based on low-resolution data) and the likelihood of magnetic reconnection occurring nearby. Thus, selections are biased toward high-shear magnetopause crossings, i.e., when the magnetosheath magnetic field is southward. Most burst mode intervals were selected at magnetopause crossings. Other burst mode intervals include regions at the magnetopause flanks (possibly unstable to the Kelvin-Helmholtz instability), the turbulent magnetosheath, and Earth's bowshock and foreshock. Burst mode intervals in the magnetosphere far from the magnetopause are uncommon.

(2) The typical Nyquist frequency of the electric field data usually prohibits investigation of waves at the plasma frequency $f_{pe} \gtrsim 32$ kHz when $n_e \gtrsim 13\,\mathrm{cm}^{-3}$, which is lower than the typical magnetosheath density. Therefore, plasma frequency waves are unlikely to be seen in the magnetosheath.

These selection biases mean that the waves we investigate are predominantly found in the magnetosphere close to the magnetopause. A smaller group of wave events is found in the electron foreshock, where the density is low enough to resolve f_{pe} in the hmfe data.

4 Observations

In this section we present examples of the types of waves found and the statistical results from our dataset, focusing on both the electrostatic and electromagnetic properties of the waves. We transform the three-dimensional electric field **E** into field-aligned coordinates, where $\mathbf{E}_{\parallel}$ is aligned with $\mathbf{B}_0$, $\mathbf{E}_{\perp 1}$ is perpendicular to $\mathbf{B}_0$ in the $\mathbf{B}_0 \times (\mathbf{X} \times \mathbf{B}_0)$ direction, where **X** is the Geocentric Solar Magnetospheric (GSM) X direction, and $\mathbf{E}_{\perp 2}$ is also perpendicular to $\mathbf{B}_0$ and completes the right-handed coordinate system. We use the same coordinate transformation for the magnetic field fluctuations **B**.

4.1 Wave examples

4.1.1 Langmuir waves

We present some of the waveforms seen by MMS near the magnetopause. As the first example, Figure 4 shows Langmuir waves observed by MMS3 and MMS4 on 2017 January 10. The spacecraft were located at [10.3, -3.8, -0.5] R_E in GSM coordinates, close to the subsolar point. The waves are found at the magnetopause, where n_e has increased above magnetospheric values. The waves observed by MMS3, shown in Figures 4a–4c, are the most intense waves observed in our dataset, with peak amplitude of $E_{\parallel} \approx 1\,\mathrm{V\,m^{-1}}$, where $E_{\parallel}$ is the electric field parallel to $\mathbf{B}_0$. For these waves $E_{\parallel} \gg E_{\perp}$, where $E_{\perp}$ is the electric field perpendicular to $\mathbf{B}_0$. MMS3 and MMS4, which were separated by $\sim 6\,\mathrm{km}$, both observed two localized waveforms. The waveforms of $E_{\parallel}$ observed by MMS3 have approximately Gaussian profiles. Similar waveforms observed in the solar wind and at Earth's foreshock were interpreted as Langmuir eigenmodes of density cavities [*Ergun et al.*, 2008; *Graham and Cairns*, 2013a]. The eigenmode model accounts for the highly localized structure of the waveforms and the Gaussian profiles, i.e., $E_{\mathrm{env}} \approx E_0 \exp(-r^2/2l^2)$, where E_{env} is the electric field envelope function. If we assume that the Langmuir waves are convected past the spacecraft at the ion bulk speed, we estimate the length scale of the wave packets observed by MMS3 to be $l \approx 20\,\lambda_D$.

The waveforms observed by MMS4 are also localized; Figure 4g shows a more complicated waveform, while Figure 4h shows a Gaussian-like waveform, similar to MMS3.

Although the Langmuir waves were observed by MMS3 and MMS4 at similar times there is no clear evidence that these are the same waveforms observed at different locations and times.

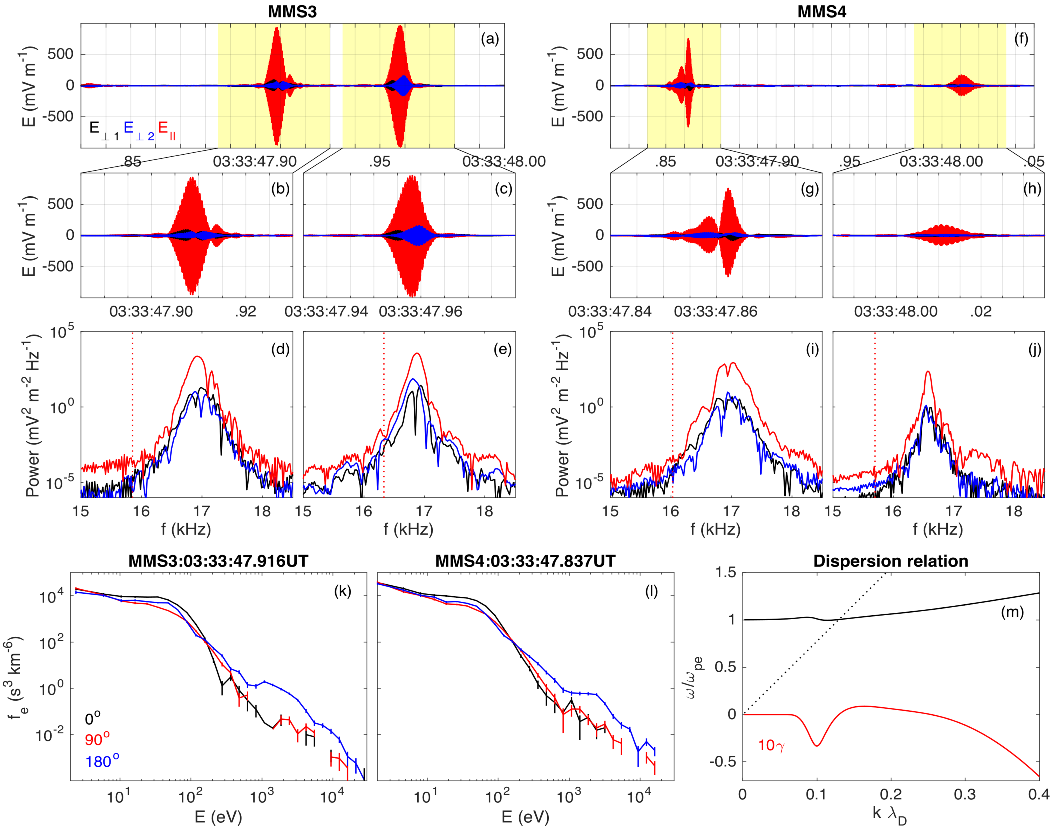

Figure 4. Langmuir waves observed by MMS3 [panels (a)–(e)] and MMS4 [panels (f)–(j)] on 2017 January 10. (a) **E** in field-aligned coordinates. (b) and (c) **E** of the two waveforms in (a). (d) and (e) Power spectra of **E** in (b) and (c). The red dotted lines indicate f_{pe}. Panels (f)–(j) Langmuir waves observed by MMS4 in the same format as (a)–(e). (k) and (l) Electron phase-space densities f_e with error bars at pitch angles $\theta = 0^\circ$ (black), 90° (red), and 180° (blue) observed by MMS3 and MMS4, respectively, around the time the Langmuir waves are observed. (m) Dispersion relation (black) and growth rate (red) predicted by a two-Maxwellian fit to the distribution in (k). For the background distribution we use $n_e = 3.3\,\mathrm{cm}^{-3}$ and $T_e = 50\,\mathrm{eV}$, and for the beam we use $n_b = 1\times10^{-2}\,\mathrm{cm}^{-3}$, $T_b = 200\,\mathrm{eV}$, and beam speed $v_b = 2.3\times10^4\,\mathrm{km\,s}^{-1}$ (1.5 keV). The dotted line indicates the electron beam speed.

The power spectra of **E** for the four waveforms are shown in Figures 4d–4e and 4g–4h. In each case the power has a very narrow peak just above f_{pe} calculated from n_e measured by FPI. The difference between the predicted f_{pe} and frequency of peak power is about 1 kHz, suggesting that the measured n_e is fairly reliable here. The finite width of the spectral peak is due to highly localized waveform. These observations are consistent with the waveforms being Langmuir waves.

Figures 4k and 4l show electron phase-space densities f_e at pitch angles $\theta = 0°$, $90°$, and $180°$ measured by MMS3 and MMS4 when the Langmuir waves are observed. Evidence for beam and plateau-like distributions are found near energies $E \sim 1$ keV, at $\theta = 180°$. Therefore, the source of the Langmuir waves is likely the usual bump-on-tail instability. Figure 4k shows evidence of $df_e/dv_{\|} > 0$ at $\theta = 180°$, suggesting an unstable electron distribution. Figure 4m shows the dispersion relation and growth rate based on a simple two-Maxwellian fit to the distribution in Figure 4k. The unstable mode is predicted to be the Langmuir wave, and has a positive growth rate due to the bump-on-tail instability.

In Figure 5 we plot three examples of the types of Langmuir-like waves we observe near the magnetopause in our dataset. In each case $E_{\|} \gg E_{\perp}$, corresponding to $F_E \approx 0$ in Figure 1a. Figures 5a–5c show an example of a very narrowband Langmuir wave observed by MMS1. The wave amplitude varies significantly over the two second interval. There are no highly localized waveforms, like those observed in Figure 4. Figures 5d–5f show a Langmuir wave with significantly broader spectral peak near f_{pe}. Figure 5e shows that the wave frequencies tend to change with position, resulting in a broader spectral peak. Figures 5g–5i shows a relatively broadband Langmuir-like wave. The power peaks at f_{pe}. Figures 5g and 5h show that the amplitudes vary rapidly with time. The fluctuations are approximately sinusoidal, so the wide spectral peak is due to the rapid variations in the wave amplitude, i.e., a rapidly changing envelope function.

Figure 5 shows that lower-frequency waves can be observed simultaneously with the Langmuir waves. In Figures 5a–5c the four lowest Bernstein waves $E_{\perp} \gg E_{\|}$ are observed. These Bernstein waves have peak frequencies just above the harmonics of f_{ce}. In Figures 5g–5i we observe electromagnetic whistler waves with $E_{\perp} \gg E_{\|}$. The whistler waves have peak frequencies centered around 500 Hz. The Langmuir-like waveforms are modulated by the electric field of the whistler waves. These Langmuir-like waves have been reported previously near the dayside magnetopause [*Reinleitner et al.*, 1982, 1983; *Gurnett and Reinleitner*, 1983], and are frequently observed in our survey. In Figures 5d–5f we observe low-amplitude broadband electrostatic fluctuations below f_{pe}. Fig-

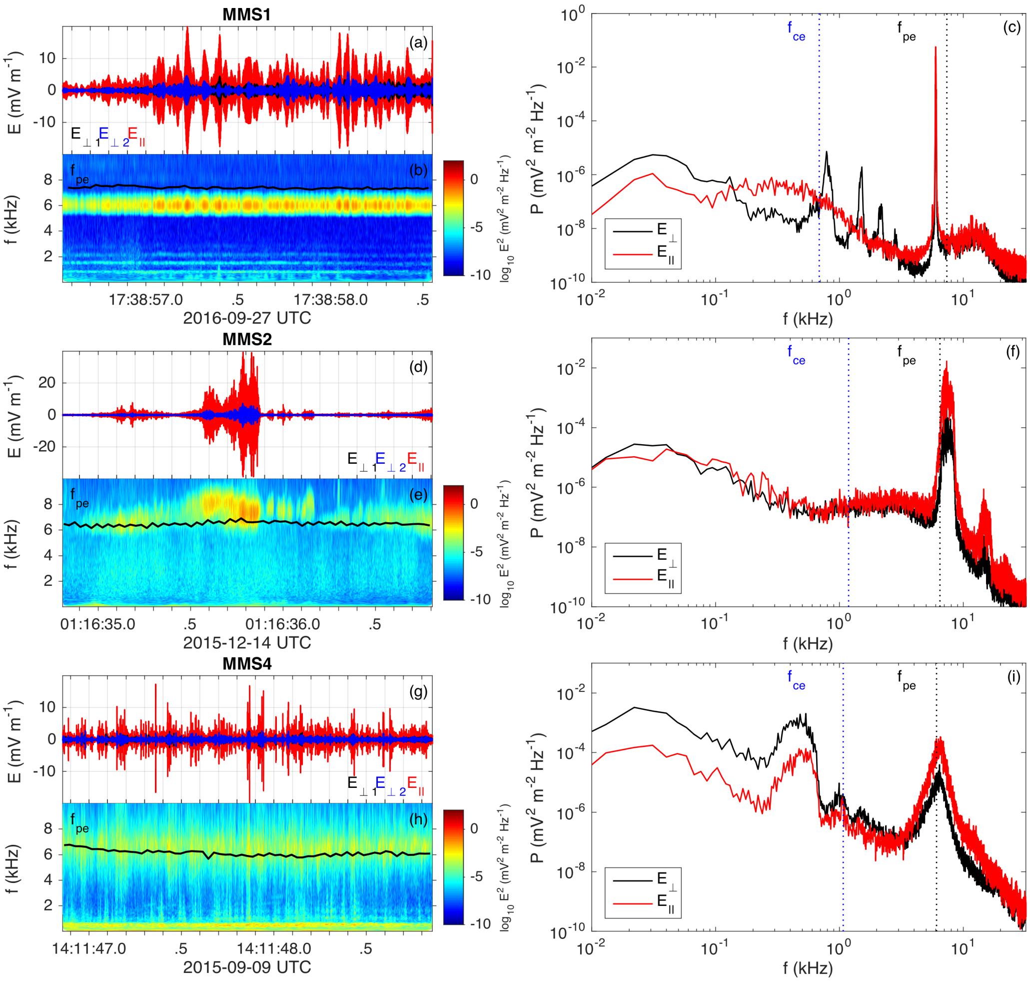

320 **Figure 5.** Three examples of Langmuir-like waves observed by MMS1 on 2016 September 27 [panels (a)–(c)], MMS2 on 2015 December 14 [panels (d)–(f)], and MMS4 on 2015 September 09 [panels (g)–(i)]. (a) **E** in field-aligned coordinates. (b) Spectrogram of **E** (the black line indicates f_{pe} and the blue line indicates f_{ce}). (c) Power spectra of $\mathbf{E}_\perp$ (black) and $\mathbf{E}_\parallel$ (red) over the wave event. (d)–(f) and (g)–(i) are in the same format as (a)–(c).

ure 5 shows that lower-frequency waves can be observed simultaneously with Langmuir-like waves, and that the spectral width of the Langmuir-like waves is quite variable. The broader spectral peak waves may correspond to beam-mode waves, rather than Langmuir waves.

We now investigate the electromagnetic properties of Langmuir waves. In some rare cases we see **B** associated with Langmuir waves near the magnetopause. Figure 6 shows two examples of Langmuir waves where **B** fluctuations are observed above the SCM noise floor.

Figures 6a–6g shows a wave event observed on 2016 October 13 by MMS1, which was located at $[4.3, 9.9, -4.6]$ R_E (GSM) in a region of density depletion. For this event $n_e = 0.07\,\mathrm{cm}^{-3}$ and $f_{pe}/f_{ce} = 1.6$. At the beginning of the event we observe Langmuir waves with $E_{\parallel} \gg E_{\perp}$, corresponding to $F_E \approx 0$. UH waves are observed toward the end of the wave event with $E_{\perp} \gg E_{\parallel}$ (Figure 6a), corresponding to $F_E \approx 1$. Figure 6b shows that the Langmuir waves have frequency $f \approx f_{pe}$. The UH waves have frequency above f_{uh}, and between $2f_{ce}$ and $3f_{ce}$. Figure 6c shows a slight enhancement of $B_{\perp}$ above the noise floor when $\mathbf{E}_{\parallel}$ is maximal. Figure 6d shows that **B** has frequency equal to $\mathbf{E}_{\parallel}$. This suggests that the Langmuir waves have a finite, but small, $k_{\perp}$, based on Figure 1d. We also observe weak **B** associated with the UH waves, primarily parallel to $\mathbf{B}_0$. Therefore, for this wave event the Langmuir and UH waves have weak electromagnetic components.

In Figure 6e we compute the ellipticity of **B**. For the Langmuir waves **B** is right-hand polarized, consistent with Figure 1f. For the UH waves the ellipticity of **B** is close to 0 (linear polarization); however, $B_{\perp}$ is small compared with the SCM noise, so the ellipticity of **B** is questionable for the UH waves. In Figure 6f we plot the spectrogram of $c|\mathbf{B}|/|\mathbf{E}|$. We find that $c|\mathbf{B}|/|\mathbf{E}| \sim 10^{-2} - 10^{-1}$ for both the Langmuir and UH waves. These values are in good agreement with theoretical predictions for $f_{pe}/f_{ce} = 1.6$ (not shown).

The second event (Figures 6h–6n) is a Langmuir wave observed by MMS2 on 2016 October 16 in the magnetosphere. The Langmuir waves reach large amplitudes, over $100\,\mathrm{mV\,m^{-1}}$. The waves have $E_{\parallel} \gg E_{\perp}$ (Figures 6i and 6n) and a narrow spectral peak just below 6 kHz. For this event the spectral peak is about 1 kHz below the predicted f_{pe}, showing that the measured n_e may be overestimated. Assuming the spectral peak corresponds to f_{pe}, we estimate $f_{pe}/f_{ce} \approx 7.7$, so the plasma is more weakly magnetized than the

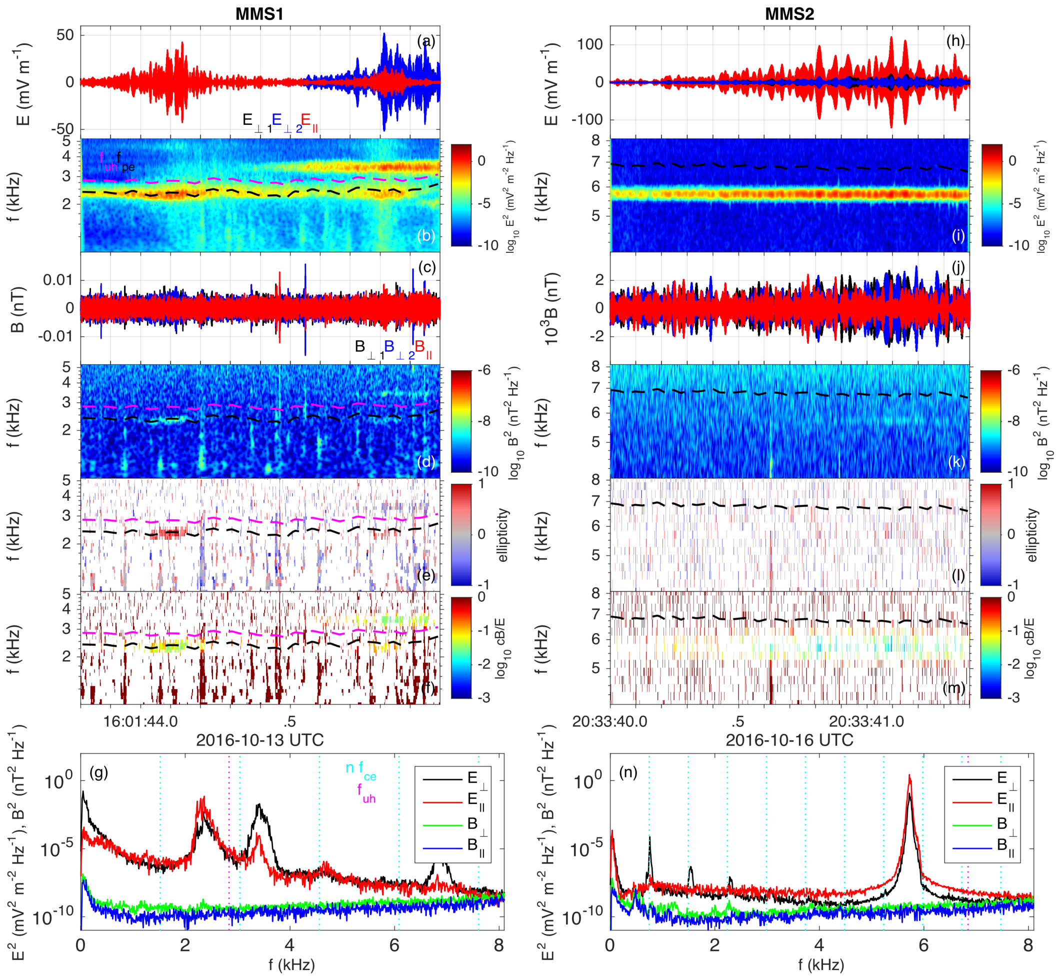

Figure 6. Two examples of **E** and **B** of Langmuir waves observed MMS1 on 2016 October 13 [panels (a)–(g)] and by MMS2 on 2016 October 16 [panels (h)–(n)]. (a) **E** in field-aligned coordinates. (b) Spectrogram of **E**. (c) **B** in field-aligned coordinates. We use a narrow bandpass filter that includes both the Langmuir and UH waves. (d) Spectrogram of **B**. (e) Spectrogram of the ellipticity of **B**. (f) Spectrogram of $c|\mathbf{B}|/|\mathbf{E}|$. The black and magenta dashed lines in panels (b) and (d)–(f) indicate f_{pe} and f_{uh}, respectively. (g) Power spectra of perpendicular and parallel components of **E** (black and red lines) and **B** (green and blue lines) over the wave event (dashed cyan lines indicate nf_{ce} and the magenta dashed line indicates f_{uh}). Panels (h)–(n) are in the same format as (a)–(g).

event in Figures 6a–6g. Figures 6j and 6k show that there is a slight enhancement in **B** at the Langmuir wave frequency. For this event the ellipticity of **B** is not clear because **B** is small compared with the SCM noise level (Figure 6m). Figure 6n shows that $c|\mathbf{B}|/|\mathbf{E}| \lesssim 10^{-2}$, meaning the waves have a weaker electromagnetic component that the event in Figures 6a–6g, but consistent with Figure 1c. Thus, the electromagnetic Langmuir wave properties, when detected, are consistent with predictions from kinetic theory.

4.1.2 Upper hybrid waves

We now present some examples of UH waves observed near Earth's magnetopause. Figure 7 shows four UH wave events. Figure 7 shows the waveforms of **E**, the spectrogram of **E**, and ellipticity of **E** for four wave events. All four events are characterized by $E_\perp \gg E_\|$ and the peak power is close to the predicted UH frequency f_{uh}. In each case the polarization of **E** exhibits both right and left-hand polarization, although on average the polarization is close to 0 (linear), as expected from Figure 1e for moderate to large $k_\perp$ UH waves. The polarizations of **E** are inconsistent with low-k Z mode waves and the left- and right-hand polarized electromagnetic waves. We note that left-hand and right-hand polarizations, as well as polarization reversals, in **E** can simply result from the superposition of waves with different **k**.

Figures 7a–7c show an example of UH wave activity close to the density gradient of the magnetopause. The density gradient is seen as the increase in f_{uh} toward the end of the wave event (Figure 7b). Figure 7a show that **E** is bursty, with very rapid fluctuations in $|\mathbf{E}|$. The most intense wave power is found just above f_{uh} and below $6f_{ce}$. In addition to the UH waves we observe electron Bernstein waves both above and below f_{uh}. Below f_{uh} the Bernstein waves have peak power at frequencies just below the f_{ce} harmonics, while above f_{uh} the Bernstein waves are more broadband with peak powers near $(n + 1/2)f_{ce}$. Figure 7b shows that the UH and Bernstein waves are unable to penetrate the density gradient. When f_{uh} starts to increase the UH and Bernstein wave activity is no longer observed. We also observe right-hand polarized whistler waves (Figures 7b–7c) at $f = 1.2$ kHz (or $f/f_{ce} = 0.7$) over the same interval as the UH and Bernstein waves.

The wave event in Figures 7d–7f is a highly localized UH wave, with peak amplitude of $\approx 120\,\mathrm{mV\,m^{-1}}$. The waveform develops in a density cavity (where $f_{uh} \approx 8f_{ce}$ is minimal). The wave power peaks near the local $f_{uh} \approx 8f_{ce}$. Two well-defined spectral

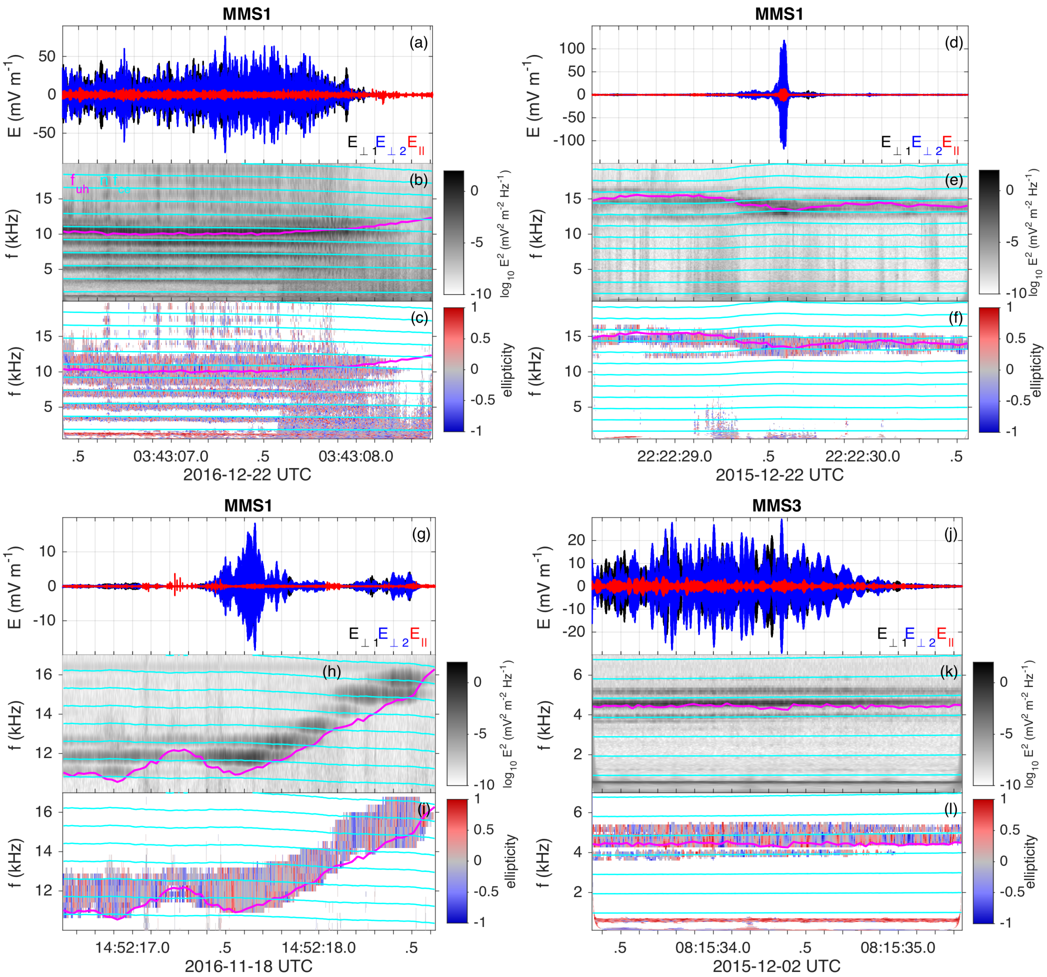

Figure 7. Four examples of UH waves observed at Earth's magnetopause by MMS1 on 2016 December 22 [panels (a)–(c)], MMS1 on 2015 December 22 [panels (d)–(f)], MMS1 on 2016 November 18 [panels (g)–(i)], and MMS3 on 2015 December 02 [panels (j)–(l)]. (a) **E** in field-aligned coordinates, (b) Spectrogram of **E**, and (c) Ellipticity of **E** (+1 is right-hand circularly polarized, −1 left-hand circularly polarized). The cyan lines in panels (b) and (c) are the harmonics nf_{ce} of the electron cyclotron frequency f_{ce} and the magenta line is f_{uh}. Panels (c)–(e), (f)–(h), and (i)–(k) present the same quantities as (a)–(c).

peaks occur near f_{uh} separated by 460 Hz (see Appendix B:), which cannot be resolved in Figure 7e. Although the waveform is highly localized, low-amplitude waves near f_{uh} persist throughout the wave event. We only observe Bernstein waves just above and just below f_{uh}, in contrast the event in Figures 7a–7c, where all Bernstein waves below f_{uh} are found.

The third UH wave event, shown in Figures 7g–7i, is observed at the magnetopause density gradient where there is a rapid increase in f_{uh} (Figure 7h). Unlike the event in Figures 7a–7c the density gradient does not arrest wave activity. Rather, the UH waves increase in frequency so the wave power has frequencies above the local f_{uh}. Figure 7h shows that the changes in frequency are discrete across the density gradient, rather than smoothly increasing with f_{uh}. The wave powers have peaks at frequencies just above the harmonics of f_{ce}. Thus, the frequency splitting is approximately equal to f_{ce}. The wave frequencies range from just above $12 f_{ce}$ to just above $18 f_{ce}$. For the UH dispersion surface the cutoff and f_{uh} change smoothly with n_e, so the discrete frequencies are unlikely to be explained by low k waves (or magnetoionic or fluid wave theories). This suggests that the waves are behaving like Bernstein waves (UH waves at large k), where the minimum frequency is determined by f_{ce}, meaning that kinetic effects are needed to explain the observed wave behavior. Because of the density gradient it is unclear if the waves lie on the UH dispersion surface or the electron Bernstein dispersion surface just above it. Figures 7g and 7h show that the wave amplitude peaks within a local density cavity. This could be the result of UH eigenmodes of a density cavity. This wave event shows that the density changes play an important role in determining the wave behavior.

The final UH wave event, shown in Figures 7j–7l, occurs over an interval where f_{uh} (and n_e) are approximately uniform. Large-amplitude bursty $\mathbf{E}$ are observed over an extended period of time (Figure 7j), similar to the event observed in Figures 7a–7c. The wave power peaks just above f_{uh} and below $5 f_{ce}$. We observe electron Bernstein waves only above $5 f_{ce}$ and near $4 f_{ce}$, close to f_{uh}. This is similar to the event in Figures 7d–7f, without the density changes. We also observe whistler waves (Figures 7k and 7l) over the entire wave event at $f \approx 600$ Hz (or $f/f_{ce} \approx 0.6$).

From the results in Figure 7 we can conclude:

(1) UH waves are observed near f_{uh}, although often not exactly at f_{uh} as expected from Figure 1. UH waves are often accompanied by electron Bernstein waves. The rela-

tive amplitudes of the different Bernstein waves, and which ones are observed, is highly variable. In some cases all possible Bernstein modes with frequencies below f_{uh} can be excited, whereas in other cases Bernstein waves are only seen near f_{uh}.

(2) The magnetopause density gradient plays an important role in determining the UH wave behavior. In some cases UH wave activity does not penetrate density gradients, while in other cases the density gradient forces the UH waves to change frequencies discretely by f_{ce}. In some cases the wave amplitude peaks in local density cavities, suggesting that the UH waves could be at least partially trapped.

(3) In some cases the UH and Bernstein waves are colocated with whistler waves (in other cases no whistler waves are observed). This may suggest that the unstable electron distributions producing UH and Bernstein waves are also unstable to whistler emission, e.g., instabilities associated with the perpendicular temperature anisotropy of hot magnetospheric electrons.

We now investigate the electromagnetic properties of UH waves observed near the magnetopause. Figure 8 shows two examples of the UH waves where **B** is clearly observed above the SCM noise floor. Figures 8a–8g show an UH wave observed near the magnetopause by MMS2 on 2016 November 14. No Bernstein waves are observed at this time. Figure 8a shows that $E_{\perp} \gg E_{\|}$, like the UH waves in Figure 7. The wave has frequency just below $f_{uh} \approx f_{pe}$ estimated from FPI electron moments, and just above $7f_{ce}$ (Figures 8b and 8g). Figures 8c and 8d show that the **B** fluctuations develop at the same time as the largest **E**. The magnetic field fluctuations are closely aligned with $\mathbf{B}_0$, i.e., $B_{\|} \gg B_{\perp}$ (corresponding to $F_B \approx 0$). The fact that $B_{\|} \gg B_{\perp}$ means that $k_{\perp} \gg k_{\|}$, as expected for UH waves. The observed **E** and **B** are consistent with Figures 1a and 1b. Figure 8e shows that $S_{\|}/S$ typically remains close to 0 as predicted by Figure 1d. Figure 8f shows that $c|\mathbf{B}|/|\mathbf{E}| \sim 10^{-2} - 10^{-1}$. This suggests that the waves have $k_{\perp}$ corresponding to the region where f peaks, i.e., where the group speed v_g is close to zero. The observed $c|\mathbf{B}|/|\mathbf{E}|$ is too small for the waves to be Z-mode; the maximum predicted $c|\mathbf{B}|/|\mathbf{E}|$ along $k_{\perp}$ for the Z-mode is 0.2 for the local plasma conditions.

The second UH wave example (Figures 8h–8n) is observed near the magnetopause by MMS4 on 2016 December 23. For this example the plasma is more strongly magnetized. The waves have frequency just above f_{uh} and just below $3f_{ce}$ (Figures 8i and 8n). We also observe Bernstein waves between f_{ce} and $2f_{ce}$ and whistler waves below f_{ce}

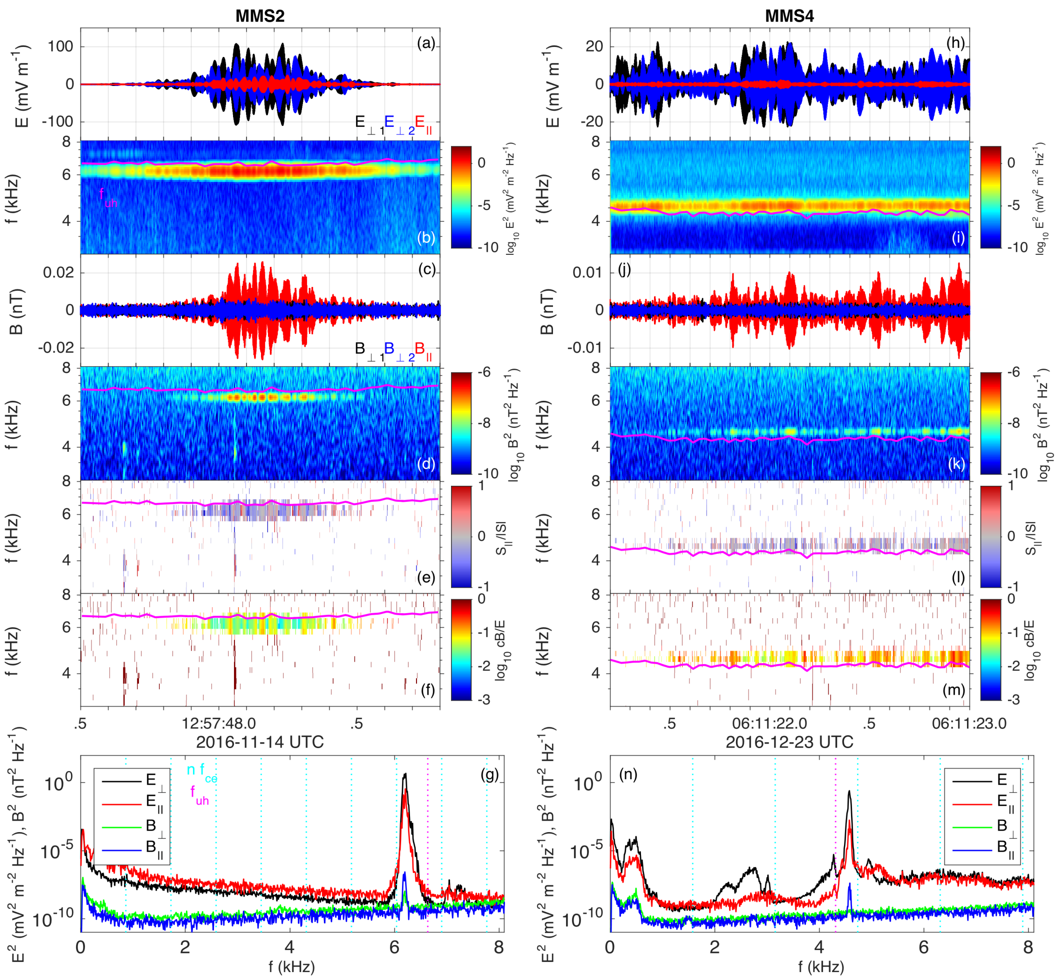

Figure 8. Two examples of **E** and **B** of UH waves observed by MMS2 on 2016 November 14 [panels (a)–(g)] and by MMS4 on 2016 December 23 [panels (h)–(n)]. (a) **E** in field-aligned coordinates. (b) Spectrogram of **E**. (c) **B** in field-aligned coordinates. (d) Spectrogram of **B**. (e) Spectrogram of $S_{\|}/S$. (f) Spectrogram of $c|\mathbf{B}|/|\mathbf{E}|$. The magenta line in panels (b) and (d)–(f) indicates f_{uh}. (g) Power spectra of perpendicular and parallel components of **E** (black and red lines) and **B** (green and blue lines) over the wave event (dashed cyan lines indicate nf_{ce} and the magenta dashed line indicates f_{uh}). Panels (h)–(n) are in the same format as (a)–(g).

(Figure 8n). Like the previous example, $E_\perp \gg E_\parallel$ and $B_\parallel \gg B_\perp$ for the UH wave. No **B** is observed for the Bernstein wave, although its amplitude is small. Figure 8l shows that $S_\parallel/S \sim 0$, consistent with UH waves. Figure 8m shows that $c|\mathbf{B}|/|\mathbf{E}| \sim 10^{-1}$, with several regions where $c|\mathbf{B}|/|\mathbf{E}| > 10^{-1}$. Thus, this wave event is more electromagnetic than the event in Figures 8a–8g. The predicted peak in $c|\mathbf{B}|/|\mathbf{E}|$ for **k** perpendicular to $\mathbf{B}_0$ is 0.39 for the local plasma conditions. We also note that the variations in **E** and **B** differ (Figures 8h and 8i), meaning that $c|\mathbf{B}|/|\mathbf{E}|$ varies with position or time. This is most evident by comparing the left-hand side of the waveform, where $E \sim 20\,\mathrm{mV\,m^{-1}}$ and **B** is negligible, with the right-hand side of the waveform, where E is also $\sim 20\,\mathrm{mV\,m^{-1}}$ and B reached $\approx 0.01\,\mathrm{nT}$. This suggests that k could vary significantly with time or position (possibly leading to mode conversion). The values of $c|\mathbf{B}|/|\mathbf{E}|$ are smaller than the maximum for the Z-mode, corresponding to large $k_\perp$. Thus, the waves are consistent with UH waves, rather than Z-mode waves.

Figure 8i also shows broadband **E** activity (above the noise floor) above f_{uh} and below $2f_{uh}$, seen most clearly at $\sim 7\,\mathrm{kHz}$. This is consistent with radio emission, and possibly nonthermal continuum radiation. Since the most intense broadband wave activity is neither observed at f_{uh} nor $2f_{uh}$, the radio emission is probably not locally generated. The polarization analysis of **E** shows that the waves are predominantly right-hand polarized, suggestive of X-mode emission (Figure 3).

4.2 Statistical results

In this subsection we present the statistical results of the high-frequency waveforms, focusing on where the waveforms are observed, their electric field properties, and the properties of their electromagnetic components.

4.2.1 Wave event locations

The locations of the wave events, detailed in section 3, are shown in Figure 9. We divide the wave events into two groups: those observed at the magnetopause and in the magnetosphere (red points) and those found in the foreshock (blue points). We define the foreshock events to be those satisfying either (1) $V_{i,x} < -200\,\mathrm{km\,s^{-1}}$, $|\mathbf{B}| < 20\,\mathrm{nT}$, and $\sqrt{Y^2 + Z^2} < 8R_E$, or (2) $d_{\mathrm{MP}} > 2R_E$ and $\sqrt{Y^2 + Z^2} < 8R_E$, where d_{MP} is the estimated distance of the wave event (detailed below) from the magnetopause (Figure 9d). These criteria were selected to minimize the number of false positives. We assume the remaining wave events correspond to the magnetopause and the magnetosphere, based on the selection biases outlined in section 3. We find 493 events at the foreshock and 8344 events at the magnetopause and in the magnetosphere, based on the above criteria. As a result of MMS's $12R_E$ apogee the foreshock waves are observed very close to the bowshock for higher than usual solar wind dynamic pressure ($\sim$ 2 nPa at 1 AU).

Figures 9a shows the wave event positions in the X–Y plane in GSM coordinates. The wave events are found all along the magnetopause, including the subsolar point and both flanks. Figures 9c shows the wave event positions in the Y–Z plane in GSM coordinates. Overall, the large-amplitude ($> 20\,\mathrm{mV\,m^{-1}}$) high-frequency waves occur at all regions along the magnetopause covered by MMS's orbit.

We now investigate statistically how close the waves are to the magnetopause. To estimate the magnetopause location we use the *Shue et al.* [1998] model [equations (10) and (11)], using the solar wind B_z (GSM) and dynamic pressure D_p from the OMNI database. For each wave event we then calculate the minimum distance d_{MP} of the wave event to the predicted magnetopause using the spacecraft location at the time of the wave event. Figure 9b shows d_{MP} versus magnetic local time (MLT) ($d_{\mathrm{MP}} < 0$ is inside the predicted magnetopause and $d_{\mathrm{MP}} > 0$ is outside). The foreshock, and magnetopause and magnetospheric events are fairly well separated from each other. As expected from the burst mode selections, most of the waves are observed near the magnetopause, with most wave events observed for $d_{\mathrm{MP}} < 0$ (magnetospheric side), and statistically d_{MP} tends to decrease toward the flanks. Figure 9d shows the histograms of d_{MP} for magnetopause and foreshock wave events. For the foreshock events the median and standard deviation of d_{MP} is $2.4 \pm 0.5\,R_E$, while for the magnetopause and magnetospheric waves it is $-0.6 \pm 0.8\ R_E$. However, the estimated d_{MP} is closer to zero near the subsolar point. Thus most waves are found at or near the magnetopause. It is unclear if such large-amplitude waves develop further inside the magnetopause because of the lack of burst mode data there.

For the foreshock wave events we estimate the shock-normal angle θ_{Bn} from the local $\mathbf{B}_0$ and the shock-normal direction based on the bowshock model in *Farris and Russell* [1994]. The median θ_{Bn} is $\approx 70^\circ$ and approximately 90% of the foreshock wave events are observed for $\theta_{Bn} > 45^\circ$, corresponding to quasi-perpendicular shocks. This is not surprising since quasi-perpendicular shocks are known to produce the electron beams re-

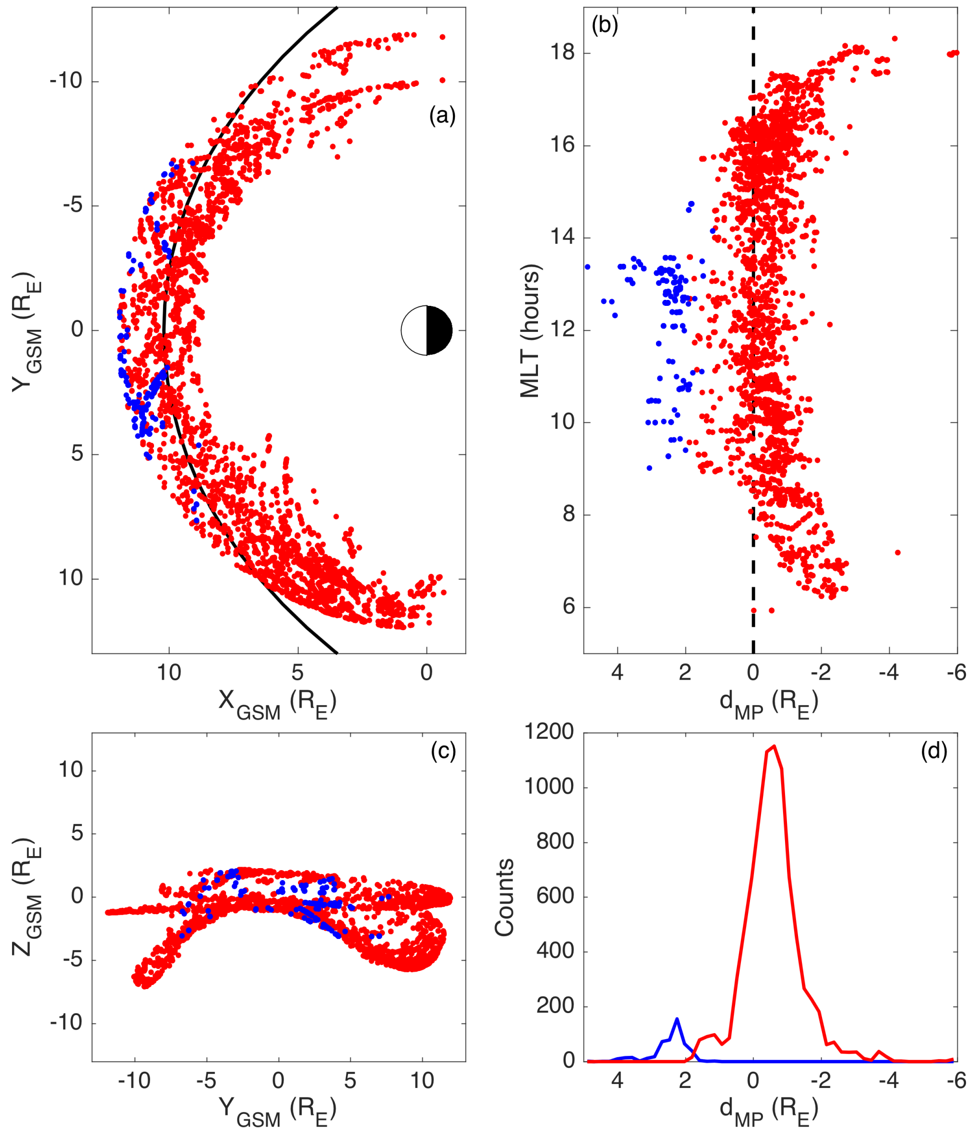

Figure 9. Location of wave events at the magnetopause and in the magnetosphere (red) and at the foreshock (blue). (a) Wave event locations in the X–Y plane in GSM coordinates. The black line is the nominal magnetopause based on the *Shue et al.* [1998] model for solar wind conditions $D_p = 2\,\mathrm{nPa}$ and $B_z = -1\,\mathrm{nT}$ (GSM). (b) Estimated distance of each wave event to the predicted magnetopause d_{MP} versus magnetic local time (MLT). Solar wind conditions are used to estimate the magnetopause location. (c) Wave event locations in the Y–Z plane in GSM coordinates. (d) Histograms of d_{MP} for magnetopause and magnetospheric events (red) and foreshock events (blue).

quired to generate Langmuir or beam-mode waves [*Fitzenreiter et al.*, 1990]. Thus, our observations are consistent with previous studies of the electron foreshock [*Filbert and Kellogg*, 1979; *Etcheto and Faucheux*, 1984]. However, SITL selection biases, which may affect the relative number of quasi-parallel and quasi-perpendicular shocks, and the typical Nyquist frequency of 32 kHz of **E** likely influence the statistical results.

We find large-amplitude waves at the magnetopause and in the magnetosphere for all orientations of $\mathbf{B}_0$ in the solar wind, which could suggest that the instabilities responsible for the waves are not strongly influenced by solar wind conditions. We note that twice as many wave events are found for $B_z < 0$ (GSM) in the solar wind compared with $B_z > 0$ (GSM) in the solar wind. This is likely the result of the selection biases of the burst mode intervals, which favor southward $\mathbf{B}_0$ in the magnetosheath, rather than the waves being more likely to be observed for solar wind $B_z < 0$, i.e., when magnetic reconnection is expected to occur near the subsolar point. We also find that many of the waves are found on closed field lines, but close to the boundary layer. Therefore, we can conclude that dayside magnetic reconnection is probably not required for large-amplitude Langmuir and UH waves to develop.

4.2.2 Electric field properties

We now investigate the properties of the wave electric fields. To investigate the nature of the waves we define the fraction of energy density in the perpendicular electric field to the total electric field energy density [*Malaspina et al.*, 2011; *Graham and Cairns*, 2014]:

$$F_E = \frac{\sum E_\perp(t)^2}{\sum E_\perp(t)^2 + \sum E_\parallel(t)^2}. \tag{1}$$

To compute F_E we high-pass filter the waveform above $f_{pe}/1.5$ to remove any lower frequency waves and sum over the entire wave event. This F_E can be compared with the predictions in Figures 1a–3a. Figure 10a shows the histogram of F_E for all wave events (black curve). Here, the counts are normalized so the maximum value is 1. We see that the wave events either have $F_E \approx 0$ or $F_E \approx 1$, corresponding to Langmuir and UH waves, respectively. There are very few wave events with intermediate values of F_E. This means that the wave vector **k** of the waves is either close to parallel or close to perpendicular to $\mathbf{B}_0$, and rarely oblique. Moreover, many of the intermediate F_E events simply result from an $F_E \approx 0$ wave and an $F_E \approx 1$ wave observed in the same wave event at different times (e.g., in Figures 6a–6g both Langmuir and UH waves are observed, and $F_E = 0.69$). The histogram of F_E for magnetospheric and magnetopause events (red curve) is similar to the histogram for all wave events, except for a smaller proportion of low F_E events (Langmuir waves). For $F_E \gtrsim 0.2$ the black and red curves approximately overlap. Near the magnetopause we find that large-amplitude UH waves ($F_E \sim 1$) are more common than Langmuir waves ($F_E \sim 0$). For the foreshock events (blue curve in Figure 10a) almost all waves have small F_E, consistent with Langmuir or beam mode waves; UH waves and/or electromagnetic Z-mode waves are unlikely to be observed at large amplitudes. These wave events are typically observed close to the bowshock, and the results may differ at greater distances from the bowshock.

We compare our results with the histogram of F_E obtained by the STEREO spacecraft in type III source regions in the solar wind at 1 AU (data from *Graham and Cairns* [2014]). The histogram of F_E differs significantly from those obtained by MMS at the foreshock and near the magnetopause. In particular, in type III source regions we observe a large proportion of intermediate values of F_E, which are not observed by MMS at the foreshock or near the magnetopause, in addition to the group of Langmuir waves with $F_E \sim 0$ similar to the foreshock. These intermediate values of F_E are interpreted as being due to the simultaneous observation of Langmuir and low wave number Z-mode waves, produced either by three-wave decay of Langmuir waves to Z-mode waves [*Graham and Cairns*, 2013b; *Kellogg et al.*, 2013; *Layden et al.*, 2013] or linear mode conversion at density perturbations [*Krauss-Varban*, 1989; *Bale et al.*, 1998; *Malaspina et al.*, 2011]. This interpretation is supported by the fact that intermediate F_E waves are correlated with faster beam speeds $v_b/v_e \gtrsim 10$ [*Malaspina et al.*, 2011; *Graham and Cairns*, 2013b; *Graham and Cairns*, 2014], meaning that the Langmuir waves are driven at lower k allowing Z-mode waves to more readily form (for the Langmuir waves in Figure 4 we estimate $v_b/v_e \approx 5$). For $v_b/v_e \lesssim 10$ low F_E Langmuir waves were consistently observed in the solar wind [*Malaspina et al.*, 2011; *Graham and Cairns*, 2014]. This suggests that the electron beams exciting Langmuir waves at the foreshock and near the magnetopause are relatively slow. In the solar wind dataset almost no waves were observed with $F_E \approx 1$, suggesting that UH waves are unlikely to be generated there, similar to the electron foreshock close to the bowshock.

Figure 10b shows the histogram of the maximum electric field strength $E_{\max}$ for UH (black) and Langmuir wave events (red). Since F_E is typically either close to 0 or 1, we

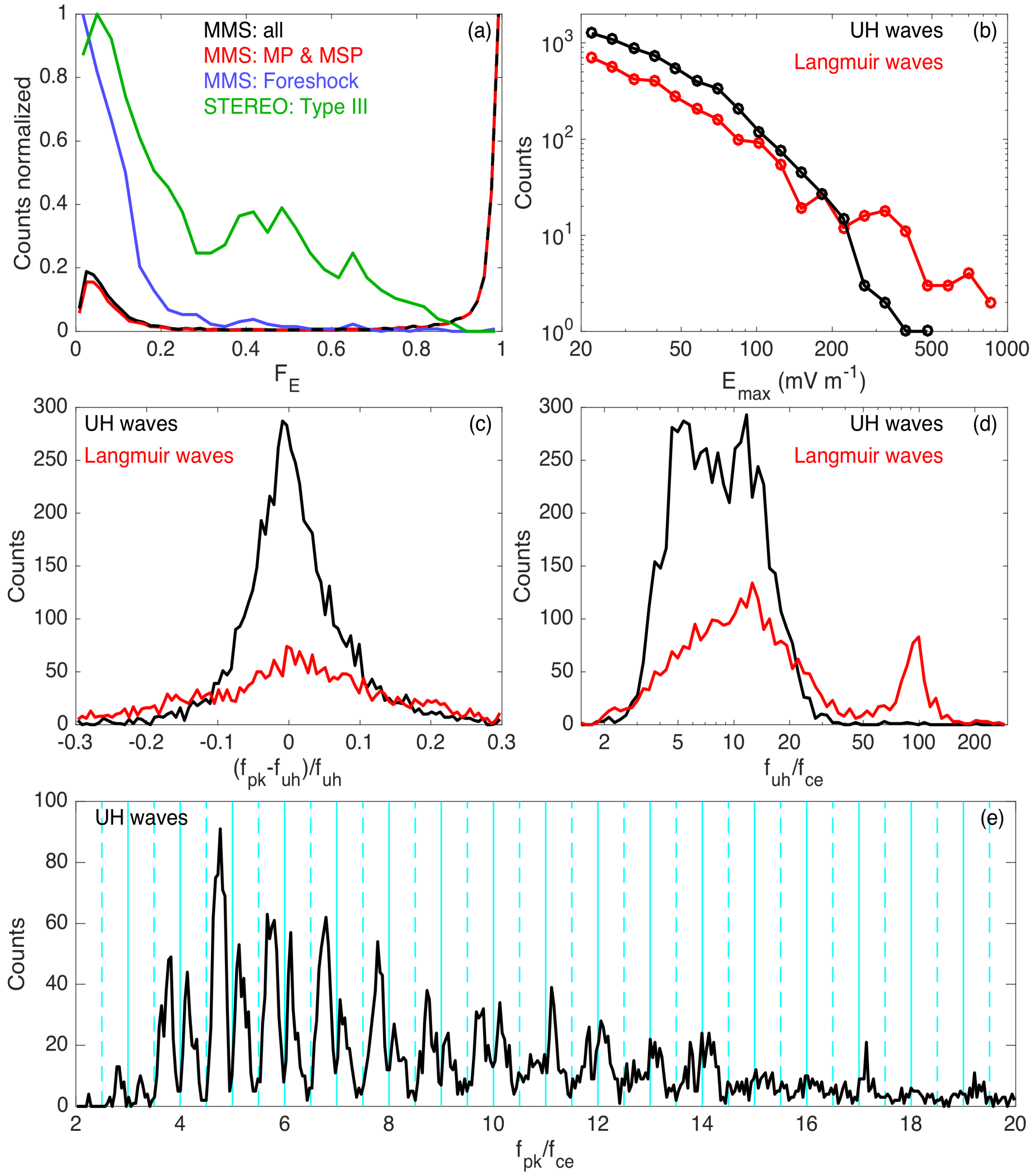

Figure 10. Statistical properties of the high-frequency waves. (a) Histograms of F_E for all wave events (black), magnetospheric and magnetopause events (red), foreshock events (blue), and Type III source region events observed by STEREO (green). For $F_E \gtrsim 0.2$ the black and red curves approximately overlap. (b) Histogram of the maximum electric field strength $E_{\max}$ for UH waves $F_E > 0.5$ (black) and Langmuir waves $F_E < 0.5$ (red). (c) $(f_{pk} - f_{uh})/f_{uh}$ for UH waves (black) and Langmuir waves (red). (d) Histograms of f_{uh}/f_{ce} for UH waves (black) and Langmuir waves (red). (e) Histograms of f_{pk}/f_{ce} for UH waves. The cyan solid and dashed lines indicate $f_{pk} = nf_{ce}$ and $f_{pk} = (n + 1/2)f_{ce}$, respectively.

define the wave events to be UH for $F_E > 0.5$ and Langmuir for $F_E < 0.5$. As expected the counts decreases as $E_{\max}$ increases for both UH and Langmuir waves. In our survey the Langmuir waves reach a maximum amplitude of $\approx 1\,\mathrm{V\,m^{-1}}$, while the UH waves reach a maximum amplitude of $\approx 500\,\mathrm{mV\,m^{-1}}$. Therefore, these waves are amongst the most intense electric fields observed at the magnetopause. For $E_{\max} \lesssim 200\,\mathrm{mV\,m^{-1}}$ UH waves are more likely to be observed than Langmuir waves, and are thus more common than Langmuir waves overall. For $E_{\max} \gtrsim 300\,\mathrm{mV\,m^{-1}}$ more Langmuir wave events are observed than UH wave events.

In Figure 10c we plot histograms of $(f_{pk} - f_{uh})/f_{uh}$ for Langmuir UH waves, where f_{pk} is the frequency at which the wave power peaks in each wave event. Here, f_{uh} is computed from the measured n_e and $|\mathbf{B}|$ when $E_{\max}$ is observed. (Using median values of n_e and $|\mathbf{B}|$ over the entire wave event interval does not qualitatively change the statistical results). For both Langmuir and UH waves the distribution of $(f_{pk} - f_{uh})/f_{uh}$ peaks around zero, indicating that the measured n_e from FPI are fairly accurate. The spread in $(f_{pk} - f_{uh})/f_{uh}$ can result from both uncertainties in n_e computed from electron moments, and the waves occurring at slightly different frequencies to f_{uh} (or f_{pe}). For instance, for electron distributions with hot and cold components UH waves can have frequencies slightly above and slightly below f_{uh} (section 5). A similar distribution of $(f_{pk} - f_{uh})/f_{uh}$ can be obtained numerically for UH waves if f_{pk} is due to UH waves and the Bernstein waves just above and below the UH dispersion relation (see section 5 for details). Some of the spread is likely due to uncertainties in the measured n_e (for very cold and dense magnetospheric electrons, n_e and hence f_{uh} can be significantly underestimated). For Langmuir wave events a wider range of $(f_{pk} - f_{uh})/f_{uh}$ is observed, which could be because these waves often have broader spectral peaks than the UH waves. In addition, beam-mode waves can have f_{pk} both above and below f_{pe} [*Fuselier et al.*, 1985]. For most Langmuir wave events $f_{pe} \approx f_{uh}$ so the distribution $(f_{pk} - f_{pe})/f_{pe}$ does not differ significantly from $(f_{pk} - f_{uh})/f_{uh}$.

In Figure 10d we plot the histograms of f_{uh}/f_{ce} for UH wave events (black) and Langmuir wave events (red). Figure 10d shows that almost all UH waves are found for $f_{uh}/f_{ce} \lesssim 22$. This corresponds to the plasma conditions on the low-density side of the magnetopause and in the magnetosphere. For the range $3 \lesssim f_{uh}/f_{ce} \lesssim 22$ large-amplitude UH waves are more likely to be observed than Langmuir or beam-mode waves. The group of Langmuir waves near $f_{uh}/f_{ce} = 100$, corresponding to solar wind conditions, are the foreshock Langmuir waves. When the plasma is more strongly magnetized, $f_{uh}/f_{ce} \lesssim 3$, more Langmuir waves are observed than UH waves, although the counts are relatively low. These results suggest that either the development of UH waves depends on f_{uh}/f_{ce}, such that UH waves are unlikely to form for very large f_{uh}/f_{ce} (such as in the magnetosheath or solar wind), or the instabilities at the magnetopause are different from those at the foreshock and in the solar wind, i.e., the unstable electron distributions responsible for UH waves rarely develop in the magnetosheath or solar wind.

In Figure 10e we plot the histogram of the ratio f_{pk}/f_{ce} for the UH wave events. Overplotted are $f_{pk} = nf_{ce}$ and $f_{pk} = (n + 1/2)f_{ce}$, indicated by the cyan solid and dashed lines, respectively. The histogram of f_{pk}/f_{ce} has distinct peaks for f_{pk} between nf_{ce} and $(n + 1/2)f_{ce}$. This is most evident for $f_{pk} \lesssim 10f_{ce}$, where the histogram of f_{pk} has minima at nf_{ce} and $(n + 1/2)f_{ce}$. In contrast, the histograms of f_{pk}/f_{ce} for Langmuir waves and f_{uh}/f_{ce} show no such minima (not shown). This shows that the wave frequencies are determined by f_{ce} and often do not exactly peak at f_{uh} (accounting for some of the spread in Figure 10c). This behavior is seen in Figures 7g–7i, where the wave frequencies discretely change by f_{ce} rather than follow $f_{uh} \approx f_{pe}$ across the density gradient. The discretized nature of the histogram of f_{pk}/f_{ce} suggests that kinetic behavior of the waves is crucial for understanding the wave properties.

Our interpretation of this behavior is the following: Most of the UH wave events are observed near the magnetopause, where the electron distributions typically consistent of hot and cold components, which modifies the dispersion relations of the UH and Bernstein waves. If we assume that f_{pk} corresponds to frequencies along the dispersion relation where the group speed is $v_g \approx 0$, so that the UH waves can locally grow to large amplitudes, we then find that f_{pk} of UH waves generally lies between $(n + 1/2)f_{ce}$ and $(n + 1)f_{ce}$. The peaks in the histogram for $nf_{ce} < f_{pk} < (n + 1/2)f_{ce}$ can develop for UH waves and the electron Bernstein waves just above f_{uh}. In addition, cyclotron damping is expected to damp UH waves with $f_{pk} = nf_{ce}$. In section 5 we show that a similar histogram of f_{pk}/f_{ce} can be obtained for electron distributions with hot and cold components. This suggests that the observed histogram can be explained by linear theory, meaning nonlinear effects may not be required to explain the observed histogram. Since hot and cold electron components are required, the associated changes in the linear dispersion relation of UH and Bernstein waves are important for investigating these waves near the magnetopause.

4.2.3 Electromagnetic properties

We now investigate the electromagnetic properties of the waves at the magnetopause and in the magnetosphere. We find that some of the wave events have **B** large enough above the SCM noise floor to calculate F_B. In our dataset approximately 20 % of the wave events are observed at frequencies resolvable by SCM (f_{pk} and f_{pe} below 8 kHz). Of these we find that 185 have **B** sufficiently high above the SCM noise floor to estimate F_B and $c|\mathbf{B}|/|\mathbf{E}|$. All these events are observed on the low-density side of the magnetopause or in the magnetosphere. We note that far more noise is found in SCM data on MMS3 than on the other MMS spacecraft. As a result very few SCM waveforms can be analyzed on MMS3, reducing our sample size. We define the fraction of perpendicular to total magnetic field energy to be

$$F_B = \frac{\sum B_\perp(t)^2}{\sum B_\perp(t)^2 + \sum B_\parallel(t)^2}. \tag{2}$$

For F_B the magnetic fields are typically small compared with the noise level so we perform narrow bandpass filtering around the wave frequency and only consider times when **B** is above the signal noise level to compute F_B.

Figure 11a shows the scatterplot of F_E versus F_B. Most wave events have $F_E \sim 1$ and F_B is typically small, with values centered around 0.2. This is consistent with UH waves with $k_\perp \gg k_\parallel$ (Figure 1). Thus, these waves cannot be L, R, or O mode waves. The waves are also unlikely to be the upper X mode because the electric fields are large amplitude and fluctuate significantly in space or time. We note the values of F_B can be increased somewhat due to the SCM noise floor, thus the actual values of F_B could be smaller than those found in the data. We find 5 events with $F_E \sim 0$ and $F_B \sim 1$, consistent with Langmuir waves with $k_\perp \ll k_\parallel$. Therefore, the observed F_B are consistent with predictions for UH and Langmuir waves.

Figure 11b shows the scatterplot of $c|\mathbf{B}|/|\mathbf{E}|$ versus f_{pk}/f_{ce}. The yellow line shows the maximum predicted $c|\mathbf{B}|/|\mathbf{E}|$ for **k** perpendicular to $\mathbf{B}_0$ versus f/f_{ce} for comparison. All observed $c|\mathbf{B}|/|\mathbf{E}|$ are below the maximum predicted $c|\mathbf{B}|/|\mathbf{E}|$, suggesting that the observed waves have larger k than the left-hand polarized Z mode (Figure 1c). We find that $c|\mathbf{B}|/|\mathbf{E}|$ is typically $\sim$ 0.05, which are relatively large values. In some cases $c|\mathbf{B}|/|\mathbf{E}| > 0.1$, corresponding to a significant electromagnetic component. We do not see any clear dependence of $c|\mathbf{B}|/|\mathbf{E}|$ on f_{pk}/f_{ce}, unlike the predicted maximum of $c|\mathbf{B}|/|\mathbf{E}|$ at low k, which decreases as f/f_{ce} increases. For UH waves the values of $c|\mathbf{B}|/|\mathbf{E}|$ cor-

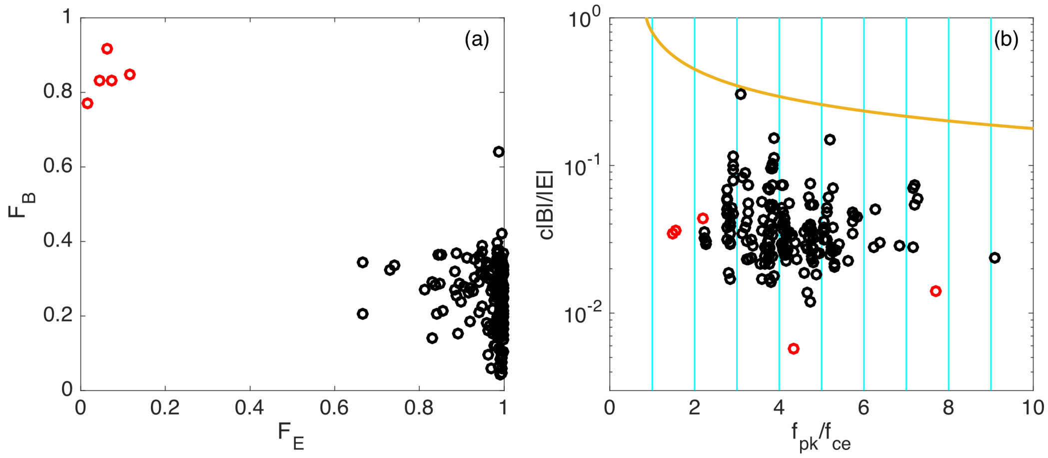

Figure 11. Electromagnetic properties of UH waves (black) and Langmuir waves (red) when **B** fluctuations are observed. (a) F_B versus F_E. (b) $c|\mathbf{B}|/|\mathbf{E}|$ versus f_{pk}/f_{ce}. The yellow line is the maximum predicted $c|\mathbf{B}|/|\mathbf{E}|$ versus f for $\mathbf{k}$ perpendicular to $\mathbf{B}_0$ and the cyan lines indicate $f_{pk} = nf_{ce}$.

respond to the range of $k_\perp$ where the frequency peaks and $v_g \approx 0$ (Figure 1c). The fact that most of the UH waves with $f_{pk} < 8$ kHz do not have **B** above the noise floor suggests that (1) the amplitude of **E** is often too small to produce **B** above the SCM noise floor for a given value of $c|\mathbf{B}|/|\mathbf{E}|$, and/or (2) the values of $c|\mathbf{B}|/|\mathbf{E}|$ are often lower than the observed values. Therefore, the values of $c|\mathbf{B}|/|\mathbf{E}|$ in Figure 11b likely represent the most electromagnetic UH waves that can be observed in our dataset. In summary, the observed electromagnetic properties of the waves are consistent with predictions for waves on the Langmuir/UH wave dispersion surface.

5 Discussion

We now try to reproduce the observed histogram of $(f_{pk} - f_{uh})/f_{uh}$ and the dependence of f_{pk} on f_{ce} numerically using linear kinetic theory. We assume that f_{pk} of UH waves, namely the frequency at which the power peaks, occurs at frequencies where $v_g \approx 0$ [*Christiansen et al.*, 1978]. In this paper we have investigated large-amplitude UH waves ($> 20\,\mathrm{mV\,m^{-1}}$), so we expect v_g to be small where the powers peak so the waves can locally grow to large amplitudes without their energy dispersing too rapidly. We note that the histogram of f_{pk}/f_{ce} (Figure 10e) is accumulated over months of data near and at the magnetopause, so the electrons distributions can differ significantly between wave events, although electron distributions with distinct temperatures are a recurring feature.

Therefore, the dependence of f_{pk} on f_{ce} should not depend strongly on the electron distribution properties, specifically the density and temperatures ratios of the hot and cold electrons n_{eh}/n_{ec} and T_{eh}/T_{ec}, and possibly the precise nature of the instability exciting the UH waves.

We reconstruct the histograms of $(f_{pk} - f_{uh})/f_{uh}$ and f_{pk}/f_{ce} numerically by assuming that f_{pk} occurs at frequencies where $v_g = 0$ in the linear dispersion relation. We solve the linear dispersion equation along $k_\perp$ to obtain the UH dispersion relation using WHAMP for the measured n_e and B_0 of each UH wave event ($F_E > 0.5$) with $f_{uh}/f_{ce} < 20$ (i.e., all the wave events used to compute the histogram in Figure 10e). This corresponds to approximately 5000 wave events. We consider two cases in detail:

(1) A single Maxwellian using the measured values of n_e, T_e, and B_0 for each wave event (termed case 1).

(2) Two Maxwellian electron distributions: a hot and cold Maxwellian with parameters $T_{eh} = 2\,\text{keV}$, $T_{ec} = 100\,\text{eV}$, $n_{eh} = 0.05n_e$, and $n_{eh} = 0.95n_e$, but using the measured n_e and B_0 for each wave event (termed case 2).

The histograms of $(f_{pk} - f_{uh})/f_{uh}$ and f_{pk}/f_{ce} are computed using all frequencies on the linear dispersion relation along $k_\perp$ where $v_g = 0$, i.e., where there is a local maximum or minimum in f. This means for case 1 we find one f_{pk} for each UH dispersion relation, while for case 2 we often find three values of f_{pk} for each dispersion relation, due to the effect of the two distinct temperatures on the linear dispersion relation (see also Appendix A:). This results in many more counts for case 2 than case 1. For case 2 we also compute f_{pk} for the nearest Bernstein wave above the UH dispersion relation (upper Bernstein wave) and the nearest Bernstein wave below the UH dispersion relation (lower Bernstein wave) using the same method.

Figure 12a shows the dispersion relations using case 2 electron parameters for values of f_{uh} between $5f_{ce}$ and $f_{uh} = 5.8f_{ce}$. The circles indicate points where $v_g = 0$. The solutions are found starting from the Z-mode cutoff at low $k_\perp$ and the dispersion relation is followed to large $k_\perp$. For $f_{uh} = 5f_{ce}$ (blue curve) the UH mode peaks near f_{uh} but does not cross f_{uh}. However, for the remaining dispersion relations with $f_{uh} > 5f_{ce}$ the UH modes cross f_{uh} as the mode transitions from the Z mode to the UH mode. For f_{uh} just above $5f_{ce}$ the UH mode spans a broad range of f for $k_\perp$ just larger than the Z-

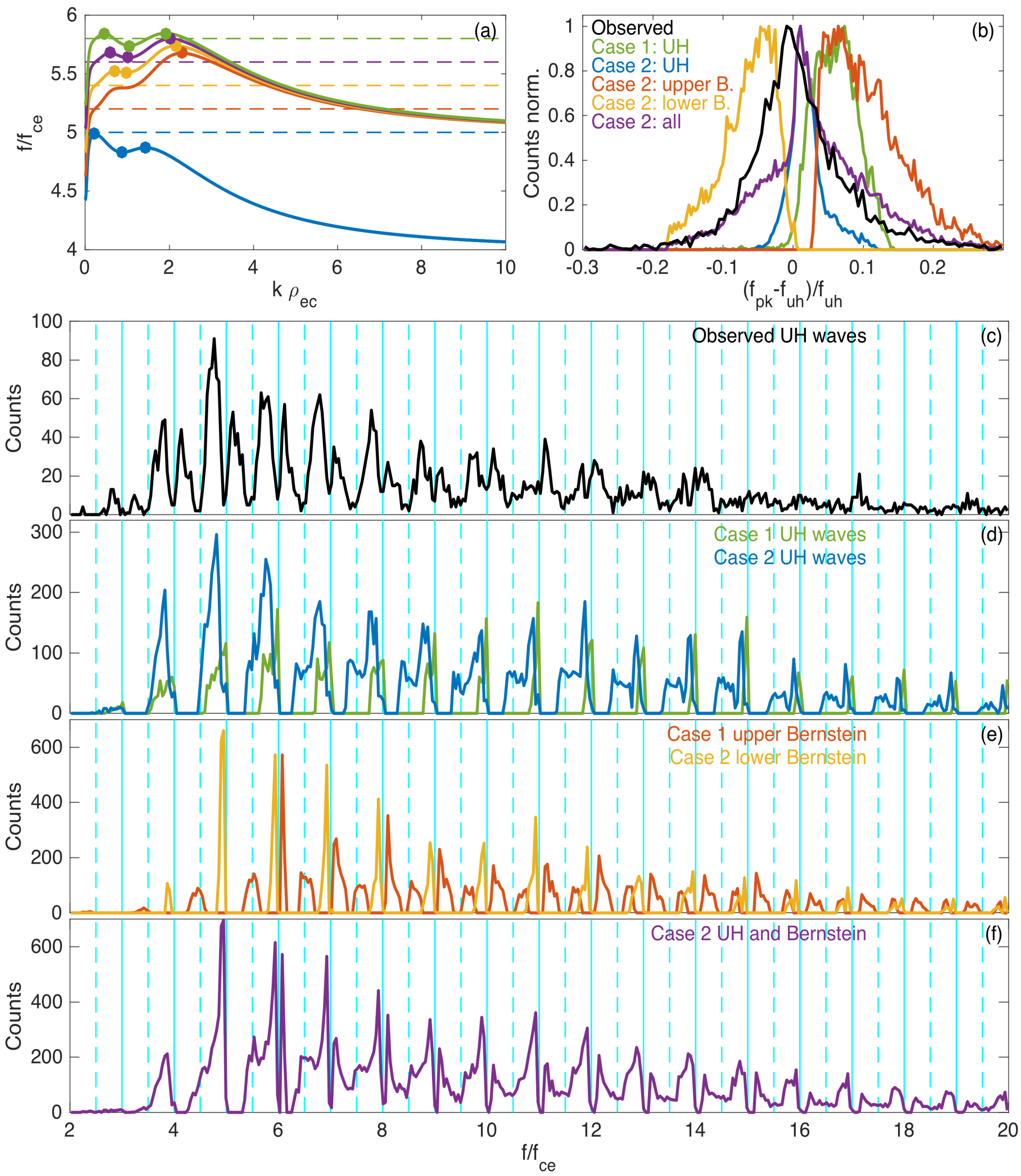

Figure 12. Histograms of f_{pk}/f_{ce} estimated from the UH dispersion relations where group velocity is zero. (a) Linear dispersion relations of UH waves for $f_{uh} = 5f_{ce}$ (blue), $5.2f_{ce}$ (red), $5.4f_{ce}$ (yellow), $5.6f_{ce}$ (purple), and $5.8f_{ce}$ (green). The colored dashed lines indicate f_{uh} for the corresponding dispersion relations and the circles indicate the points of zero group velocity. We use $B_0 = 50$ nT and $n_{ec} = 0.95n_e$, $n_{eh} = 0.05n_e$, $T_{ec} = 100$ eV, and $T_{eh} = 2$ keV. (b) Histograms of $(f_{pk} - f_{uh})/f_{uh}$ for the observed UH waves (black), case 1 UH waves (green), case 2 UH waves (blue), case 2 upper Bernstein waves (red), and case 2 lower Bernstein waves (yellow). The purple curve is the histogram of all case 2 UH and Bernstein waves. (c) Histogram of f_{pk}/f_{ce} for the observed UH waves ($F_E > 0.5$) [reproduced from Figure 10e]. (d) Histogram of f_{pk}/f_{ce} for case 1 UH waves (green) and case 2 UH waves (blue). (e) Histograms of f_{pk}/f_{ce} for case 2 upper Bernstein waves (red) and lower Bernstein waves (yellow). (f) Histogram of f_{pk}/f_{ce} for all case 2 UH and Bernstein waves (purple). The cyan solid and dashed lines in (c)–(f) indicate $f_{pk} = nf_{ce}$ and $f_{pk} = (n + 1/2)f_{ce}$, respectively.

mode, while for $f_{uh} = 5f_{ce}$ and just below $6f_{ce}$ the UH modes have a relatively narrow range of f. Overall, the UH dispersion relation depends strongly on f_{uh}/f_{ce}. In general, the UH waves have two local maxima and one local minimum in f; in some cases (e.g., $f_{uh} = 5.2f_{ce}$ in Figure 12a) only one local maximum is observed for these n_{eh}/n_{ec} and T_{eh}/T_{ec}.

We now use the numerical values of f_{pk} to determine whether they can account for the histogram of $(f_{pk} - f_{uh})/f_{uh}$ for the observed UH waves in Figure 10c (replotted in Figure 12b as the black curve). In Figure 12b we plot the histograms of $(f_{pk} - f_{uh})/f_{uh}$ for case 1 UH waves (green), case 2 UH waves (blue), case 2 upper Bernstein waves (red), case 2 lower Bernstein waves (yellow), and all case 2 UH and Bernstein waves (purple). The maximum counts of each histogram have been normalized to 1, so the spreads in $(f_{pk} - f_{uh})/f_{uh}$ for each histogram can be compared. The observed $(f_{pk} - f_{uh})/f_{uh}$ peaks near zero, and comparable numbers of positive and negative $(f_{pk} - f_{uh})/f_{uh}$ are found. For case 1 UH waves $(f_{pk} - f_{uh})/f_{uh}$ is typically larger than the observed values, and $(f_{pk} - f_{uh})/f_{uh}$ is typically positive. Thus, the prediction from a single Maxwellian distribution is inconsistent with observations.

For case 2 UH waves the histogram of $(f_{pk} - f_{uh})/f_{uh}$ is in much better agreement with observations. The histogram peaks for f_{pk} just above f_{uh}, with most values of $(f_{pk} - f_{uh})/f_{uh}$ being greater than zero, although a significant number of $(f_{pk} - f_{uh})/f_{uh}$ have negative values. The histograms of the upper and lower Bernstein waves naturally have $(f_{pk} - f_{uh})/f_{uh} > 0$ and $(f_{pk} - f_{uh})/f_{uh} < 0$, respectively. The histogram of all case 2 UH and Bernstein waves agrees well with observations, with similar spreads in $(f_{pk} - f_{uh})/f_{uh}$. Additional spread in the observed histogram of $(f_{pk} - f_{uh})/f_{uh}$ will develop due to uncertainties in the measured n_e. Overall, the observed histogram $(f_{pk} - f_{uh})/f_{uh}$ is consistent with the UH waves and some Bernstein waves for a plasma with hot and cold components.

We now compare the numerical histograms of f_{pk}/f_{ce} with the observed histogram (replotted in Figure 12c). In Figure 12d we plot the histograms of f_{pk}/f_{ce} for cases 1 (green curve) and case 2 (blue curve) UH waves. For case 1 the histogram of f_{pk}/f_{ce} has a range of values for f_{pk} between $(n + 1/2)f_{ce}$ and $(n + 1)f_{ce}$ for small f_{pk}/f_{ce}, while for larger f_{pk}/f_{ce} we find that f_{pk} always has values just below nf_{ce} in a narrow frequency range. Such a histogram is inconsistent with the observed histogram of f_{pk}/f_{ce}

in Figure 12c. The histogram of f_{pk}/f_{ce} for case 2 UH waves provides better agreement with observations. For low f_{pk}/f_{ce} we find that the counts peak for f_{pk} between $(n+1/2)f_{ce}$ and $(n+1)f_{ce}$. For $f_{pk}/f_{ce} \lesssim 10$ these peaks look quite similar to observations. For larger f_{pk}/f_{ce} we start to see a secondary peak in the counts for f_{pk} near and sometimes just below $(n+1/2)f_{ce}$. These results show that the UH dispersion relations predicted from a single Maxwellian electron distribution cannot model the observed histogram. The two-component electron distribution provides much better agreement with observations. Thus, the modification in the UH dispersion relation due to non-Maxwellian electron distributions, specifically a plasma with hot and cold electron components, is crucial for explaining the observed histogram of f_{pk}/f_{ce}. The lack of clear peaks for f_{pk} between nf_{ce} and $(n+1/2)f_{ce}$ may suggest that UH waves alone cannot explain the observed histogram.

We propose that the peaks in counts for f_{pk} between nf_{ce} and $(n+1/2)f_{ce}$ can develop when the Bernstein waves just above and below the UH dispersion relation (in particular the upper Bernstein waves) are included. In Figure 12e we plot the histograms of f_{pk}/f_{ce} for the upper (red curve) and lower Bernstein waves (yellow curve). The lower Bernstein waves yield peaks in the counts of f_{pk} just below nf_{ce}, similar to the UH waves. In contrast, the upper Bernstein waves produce can produce peak counts for f_{pk} between nf_{ce} and $(n+1/2)f_{ce}$, as well as for f_{pk} between $(n+1/2)f_{ce}$ and $(n+1)f_{ce}$. Thus, the peaks in the counts for f_{pk} just above nf_{ce} can be accounted for if the upper Bernstein waves reach amplitudes larger than the UH waves in some cases (Appendix B:). The histogram of f_{pk}/f_{ce} for both UH and Bernstein waves (Figure 12f) shows peaks in the counts of f_{pk}/f_{ce} developing for f_{pk} between both nf_{ce} and $(n+1/2)f_{ce}$ and $(n+1/2)f_{ce}$ and $(n+1)f_{ce}$, consistent with observations. We note that for $f_{pk}/f_{ce} < 5$ we are unable to reproduce the peaks for f_{pk} between nf_{ce} and $(n+1/2)f_{ce}$. There are several possible reasons for this: (1) These f_{pk}/f_{ce} correspond to very low density so n_e measured by FPI, and hence f_{uh}, becomes more uncertain. (2) When the density is very low the parameters used may not be appropriate; in particular, the plasma may be dominated by hot electrons, rather than cold electrons, thus modifying the predicted linear dispersion relations. This requires further investigation. Nevertheless, by using an electron distribution consisting of hot and cold electron distributions and including the upper and lower Bernstein waves we are able to reproduce many of the features of the observed histogram of f_{pk}/f_{ce}.

These results suggest: (1) The modification in the dispersion relation due to not-Maxwellian electron distribution is important when investigating UH and Bernstein waves near the magnetopause. In particular, distinct temperature components need to be taken into account. (2) The most intense waves near f_{uh} are not necessarily UH waves, but could be one of the Bernstein modes near f_{uh}. (3) The observed histogram of f_{pk}/f_{ce} can be explained by linear theory. Nonlinear processes do not necessarily need to be invoked to explain the observations. This suggests that the wave amplitude is not crucial, and that such behavior should be found for lower-amplitude UH and Bernstein waves near f_{uh}.

In summary, the observed histograms of f_{pk}/f_{ce} and $(f_{pk} - f_{uh})/f_{uh}$ can be explained by linear theory for electron distributions with hot and cold components. In particular, these histograms can be well modeled when UH waves and Bernstein waves near f_{uh} are considered. We therefore expect to see evidence of both UH waves and Bernstein waves near f_{uh} with large amplitudes. Appendix B: presents two examples of large-amplitude UH waves and one of the Bernstein waves near f_{uh}, showing that Bernstein waves can also grow to very large amplitudes. We are unable to reproduce the statistical results using a single Maxwellian distribution, thus emphasizing the importance of these multi-component electron distributions in determining the dispersion properties of the waves.

We can also compare the observed $c|\mathbf{B}|/|\mathbf{E}|$ in Figure 11b with numerical predictions using method above. Using WHAMP we calculate $c|\mathbf{B}|/|\mathbf{E}|$ and the associated frequency where $v_g = 0$. As input we use the local plasma conditions for all UH wave events, which satisfy $f_{pk} < 8$ kHz and $f_{pe} < 8$ kHz. We consider cases 1 (single electron Maxwellian) and 2 (two electron Maxwellians with fixed temperatures), as defined above. Figure 13 shows the observed $c|\mathbf{B}|/|\mathbf{E}|$ versus f_{pk}/f_{ce} and the numerical predictions for $c|\mathbf{B}|/|\mathbf{E}|$ at the points where $v_g = 0$. The maximum predicted $c|\mathbf{B}|/|\mathbf{E}|$ for $\mathbf{k}$ perpendicular to $\mathbf{B}_0$ is also overplotted (yellow curves).

Figures 13a and 13b show scatterplots of $c|\mathbf{B}|/|\mathbf{E}|$ and f_{pk}/f_{ce} for the results of cases 1 and 2, respectively. The yellow lines indicate the maximum $c|\mathbf{B}|/|\mathbf{E}|$, which decreases as f/f_{ce} increases. These values of $c|\mathbf{B}|/|\mathbf{E}|$ occur at low $k_\perp$, where the wave is Z-mode-like (Figure 1c) and is well approximated by magnetoionic theory. Thus, they are approximately independent of T_e and unaffected by the hot electron component used for Figure 13b. The values of $c|\mathbf{B}|/|\mathbf{E}|$ where $v_g = 0$ (red points) agree very well with observations for both cases 1 and 2. In this case the values of $c|\mathbf{B}|/|\mathbf{E}|$ are affected by T_e because the values of $k_\perp$ where $v_g = 0$ depend on T_e as well as f_{uh}/f_{ce}. This can be seen by the spread in these points in Figure 13a compared with Figure 13b, where the electron temperatures are fixed. For both cases 1 and 2 the value of $c|\mathbf{B}|/|\mathbf{E}|$ where $v_g = 0$, depends strongly on f_{uh}/f_{ce}, and hence f_{pk}/f_{ce}. In particular, as f_{pk} (and f_{uh}) approaches f_{ce} the values of $c|\mathbf{B}|/|\mathbf{E}|$ increase and can approach the maximum $c|\mathbf{B}|/|\mathbf{E}|$ (most evident in Figure 13b). However, for $f_{pk} \approx nf_{ce}$ cyclotron damping should be strong, so these points are unlikely to be observed. Most values of $c|\mathbf{B}|/|\mathbf{E}|$ are below 0.1, consistent with observations.

In Figures 13c and 13d we plot the values of $c|\mathbf{B}|/|\mathbf{E}|$ versus f_{pk} for the Bernstein waves just below and above the UH waves, respectively. For both Bernstein waves the predicted $c|\mathbf{B}|/|\mathbf{E}|$ are smaller than for the UH waves. For the upper Bernstein waves the predicted $c|\mathbf{B}|/|\mathbf{E}|$ are consistently smaller than observations. For the lower Bernstein waves $c|\mathbf{B}|/|\mathbf{E}|$ can reach observable values in rare cases. This suggests that when $c|\mathbf{B}|/|\mathbf{E}|$ can be seen by MMS the waves are likely UH rather than Bernstein. In brief, the observed values of $c|\mathbf{B}|/|\mathbf{E}|$ are consistent with predictions from linear kinetic theory. The measured values of $c|\mathbf{B}|/|\mathbf{E}|$ agree with values of $c|\mathbf{B}|/|\mathbf{E}|$ obtained at $k_\perp$ where $v_g = 0$, consistent with the results in Figure 12.

Given the very large amplitude of some of the waves, in particular the Langmuir waves, one might expect that strong turbulence processes may occur. However, despite the very-large amplitude of the most intense waves there is no clear evidence of wave packet collapse or strong turbulence processes, such as modulational instabilities [*Zakharov*, 1972]. For instance, in the limit of $T_i \rightarrow 0$, the threshold for wave packet collapse of Langmuir waves is $\Theta = W_{\max}(l/\lambda_D)^2 \gtrsim 90$ [*Graham et al.*, 2012], where $W_{\max} = \epsilon_0 E_{\max}^2/4n_e k_B T_e$ is the normalized energy density and l is the characteristic length scale of the wave packet, assumed to have the electric field profile given by $E_{\text{env}} \approx E_0 \exp(-r^2/2l^2)$. The collapse threshold increases significantly with T_i/T_e. As an example we investigate in detail the waveforms in Figure 4 observed by MMS3, which have the largest amplitude $\mathbf{E}$ observed in our dataset. By assuming an approximately Gaussian profile of $E_{env} = E_0 \exp(-r^2/2l^2)$, we estimate that $l \approx 20\,\lambda_D$ for the waveforms in Figures 4b and 4c. We then obtain $\Theta \approx 20$ and 30 for these waveforms, where $W_{\max} \approx 7 \times 10^{-2}$ for both cases. These values of $W_{\max}$ are extremely large, but l is quite small. Therefore, although the

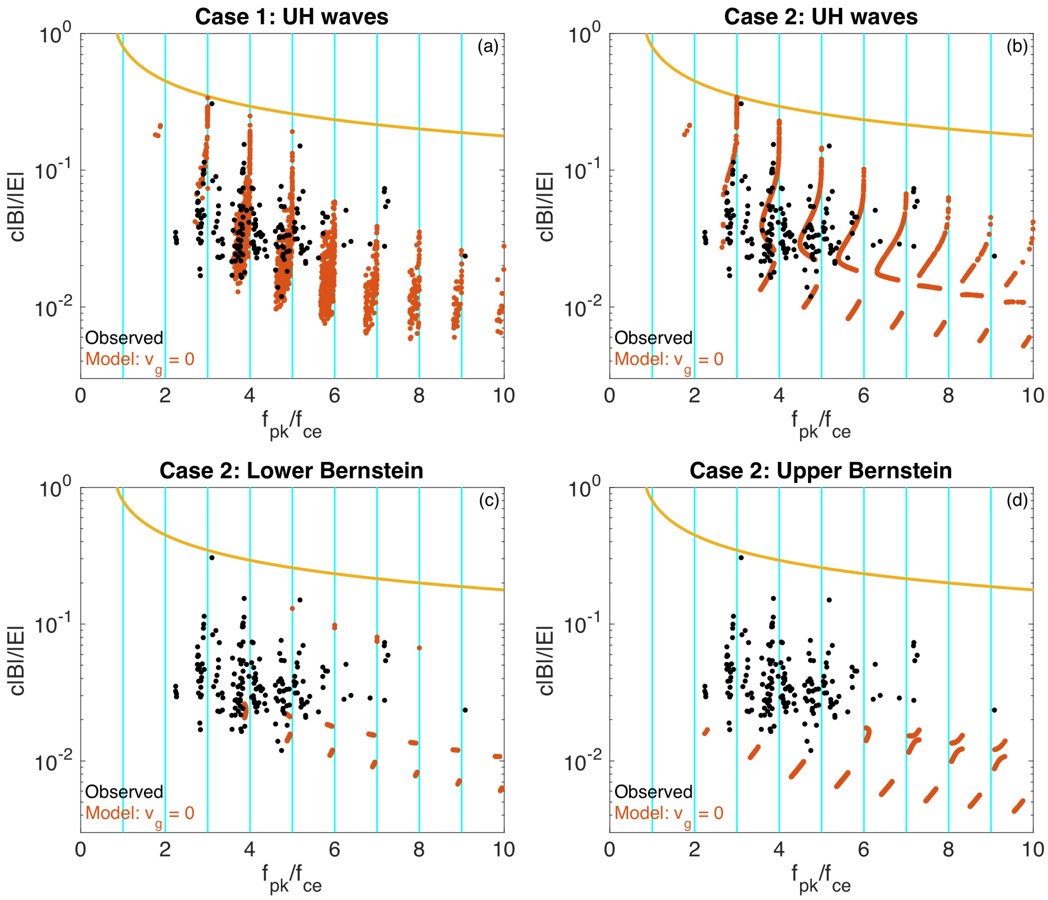

900 **Figure 13.** Comparison of observed and predicted $c|\mathbf{B}|/|\mathbf{E}|$ versus f_{pk}/f_{ce} for UH waves. (a) $c|\mathbf{B}|/|\mathbf{E}|$
901 for case 1 UH waves. (b) $c|\mathbf{B}|/|\mathbf{E}|$ for case 2 UH waves. (c) $c|\mathbf{B}|/|\mathbf{E}|$ for case 2 lower Bernstein waves. (d)
902 $c|\mathbf{B}|/|\mathbf{E}|$ for case 2 upper Bernstein waves. The black points are the observations, the red points are $c|\mathbf{B}|/|\mathbf{E}|$
903 and f/f_{ce} where $v_g = 0$. The cyan lines indicate $f_{pk} = nf_{ce}$. The yellow lines are the maximum predicted
904 $c|\mathbf{B}|/|\mathbf{E}|$ of UH waves versus f/f_{ce} for $\mathbf{k}$ perpendicular to $\mathbf{B}_0$.

waveforms are very large amplitude and are highly localized, the waves are inconsistent with wave packet collapse and strong turbulence. Since these waves have the largest amplitude **E** and $W_{\max}$ observed in our dataset, the other wave events are also unlikely to be undergoing wave packet collapse unless l is quite large. Since these very large amplitude waves are rare, it is unlikely that strong turbulence processes play any significant role at Earth's magnetopause.

In this paper we have found that large-amplitude UH and Langmuir waves are commonly observed near Earth's magnetopause, and investigated the properties of these waves. The results in this paper raise a number of questions, which require further investigation. These include:

(1) Are the observed Langmuir and upper hybrid waves a viable source of radio emission at the magnetopause? Langmuir waves can produce radio waves via linear mode conversion to Z-mode waves and subsequently to O or X mode waves [*Kim et al.*, 2007], or nonlinear three-wave processes, such as electromagnetic decay [*Cairns*, 1987], and electrostatic decay and coalescence [*Cairns and Melrose*, 1985]. Similarly, the UH waves can undergo linear mode conversion [*Oya*, 1971; *Budden and Jones*, 1987] and three-wave processes [*Melrose*, 1981]. The waveforms are observed near or at the magnetopause, where there are gradients in n_e and $|\mathbf{B}|$, making linear mode conversion a possible source of radio emission. Previous observations and theoretical studies suggest that the magnetopause may be a source of nonthermal continuum radiation in the magnetosphere [*Kurth et al.*, 1981; *Jones*, 1987; *Schleyer et al.*, 2014].

(2) What instabilities are responsible for the observed waves? How do the unstable electron distributions develop, and therefore under what magnetospheric conditions do the waves develop? Based on observations the source of the Langmuir waves is the usual bump-on-tail instability. The UH waves are often observed in plasmas with distinct hot and cold electron populations, with perpendicular temperature anisotropy observed for the hot population with energies $E \sim 1$ keV (see Appendix B: for examples). This suggests that temperature anisotropy, ring distributions, or weak loss cones of the hot magnetospheric electrons are possible sources of instability. Such distributions can also be unstable to whistler waves, which would account for why whistlers are often observed simultaneously with UH and Bernstein waves (e.g., Figure 7).

(3) What role does magnetic reconnection play in the generation of the observed waves? Magnetopause reconnection is known to produce electron beams and loss-cone distributions so nearby reconnection could account for the generation of both Langmuir and UH waves. However, many wave events are observed on closed field lines, suggesting that magnetic reconnection is often not playing a direct role in many cases.

(4) Do the observed waves contribute to electron heating or cross-field electron diffusion? And is there a correlation between these waves and enhanced superthermal electron fluxes seen near the magnetopause? A correlation between enhanced energetic electron fluxes and whistler waves has been noted near the magnetopause [*Jaynes et al.*, 2016]; such a correlation could also exist for UH and Langmuir waves (which are often colocated with whistler waves).

(5) What role do cold electrons play in determining wave properties and possible instabilities? Cold electron distributions are known to determine which Bernstein modes can be excited and their relative amplitudes [*Ashour-Abdalla and Kennel*, 1978], so the properties of the cold electron population could determine which Bernstein waves are observed near the magnetopause.

(6) In most cases harmonic signals are found in the **E** data, when harmonic frequencies can be resolved. Harmonic fields are found for both Langmuir and UH waves. These harmonic fields may be instrumental in nature; however, various physical processes are known to produce harmonic electric fields, such as nonlinear currents [*Malaspina et al.*, 2013], sheath rectification [*Boehm et al.*, 1994; *Graham et al.*, 2014], weak turbulence quasi-modes [*Yoon et al.*, 2003], and electron trapping [*Kellogg et al.*, 2010]. Therefore, it is important to determine whether the harmonic fields are physical, and if so, which processes are responsible.

Finally, this study can be extended to including plasma frequency waves observed at the night-side magnetopause and in the magnetotail. The low values of f_{pe} in these regions may enable more detailed investigation of the electromagnetic properties of these waves. We plan to investigate this in future studies.

6 Conclusions

In this paper we have presented an overview of waves at the electron plasma frequency observed by MMS at and near Earth's magnetopause.

The key results of this paper are:

(1) Large-amplitude waves with frequency $f \approx f_{pe}$ or f_{uh} are frequently observed near Earth's magnetopause, and account for some of the largest observed electric fields at the magnetopause. The waves are observed at all regions of the magnetopause covered by MMS's orbit, including the dawn and dusk flanks and the subsolar magnetopause.

(2) The waves are generally consistent with either perpendicular propagating upper hybrid waves, and field-aligned Langmuir or beam-mode waves. The waves have either $k_{\|} \gg k_{\perp}$ or $k_{\perp} \gg k_{\|}$; very few waveforms are consistent with oblique $\mathbf{k}$. In addition, we often observe electron Bernstein waves below and above the local electron plasma frequency.

(3) For magnetospheric conditions large-amplitude upper hybrid waves are more likely to be found than Langmuir or beam-mode waves. For weakly magnetized plasmas, $f_{uh}/f_{ce} \gtrsim 30$, upper hybrid waves are unlikely to be seen.

(4) The upper hybrid waves tend to avoid the frequencies $n f_{ce}$ and $(n+1/2) f_{ce}$, and as a result often do not have frequencies equal to f_{uh}. This is, in part, due to the modification in the linear dispersion relation of upper hybrid and Bernstein waves due to multi-component magnetospheric electron distributions, which typically have distinct hot and cold electron components. The large amplitude waves have frequencies consistent with zero group velocity points on the dispersion surface.

(5) In some cases the magnetic field fluctuations associated with UH and Langmuir waves are resolved. For UH waves the magnetic field fluctuations are parallel to the background magnetic field. The electromagnetic component of the UH waves can become large, with $c|\mathbf{B}|/|\mathbf{E}|$ reaching values of ~ 0.1. The observed values of $c|\mathbf{B}|/|\mathbf{E}|$ are consistent with predictions for UH waves and are too small to be associated with the low wave number Z-mode wave. In rare cases a right-hand polarized magnetic field is observed with Langmuir waves, indicating that Langmuir waves can have a weak electromagnetic component. The electromagnetic properties of both UH and Langmuir waves are consistent with predictions from linear kinetic theory.

Acknowledgments

We thank the entire MMS team and instrument PIs for data access and support. This work was supported by the Swedish National Space Board, grant 175/15. We acknowledge support from the ISSI team *MMS and Cluster Observations of Magnetic Reconnection*. MMS data are available at https://lasp.colorado.edu/mms/sdc/public. OMNI data are available at https://omniweb.gsfc.nasa.gov.

A: Upper hybrid wave properties for a two component electron distribution

In the magnetosphere and at the magnetopause the electron distributions are not well modeled as a single Maxwellian. In particular, the observed electron distributions typically have distinct hot and cold components, which modifies the dispersion relation of the UH waves (and nearby Bernstein waves). As an example, Figure A.1 shows the UH/Langmuir dispersion surface for total density $n_e = 0.5\,\mathrm{cm}^{-3}$ and $B_0 = 50\,\mathrm{nT}$ (the same conditions as Figure 1), with a hot and cold electron distribution. For the cold population we use $n_{ec} = 0.95 n_e$ and $T_{ec} = 100\,\mathrm{eV}$ and for the hot population we use $n_{ec} = 0.05 n_e$ and $T_{ec} = 2\,\mathrm{keV}$.

The most significant change to the UH dispersion relation ($k_\perp \gg k_\|$) is that there are two local peaks in frequency (and a minimum between them). Therefore, there are now three points along $k_\perp$, excluding $k = 0$, where $v_g = 0$ for UH waves, instead of one for a single Maxwellian. The Langmuir waves are similarly distorted by the two electron temperatures. However, the other properties of the dispersion surface remain similar to Figure 1. In particular, F_E and F_B are essentially unchanged. Minor changes to the wave properties include:

(1) $S_\|/S$ becomes 1 in the regions between the two frequency peaks of the UH waves. Note that in Figure 8 $S_{||}/S \sim 0$, which might suggest that the waves have $k_\perp$ near or below the first maximum in f. For the peak in f at larger $k_\perp$, $c|\mathbf{B}|/|\mathbf{E}|$ is small, so $\mathbf{B}$ may not be observed above the SCM noise floor, and thus the $S_{||}/S$ may not be measurable at these larger values of $k_\perp$.

(2) The ellipticity of $\mathbf{B}$ becomes left-hand for $k_\perp$ between the two peaks in f. However, this occurs for near-zero F_B, corresponding to $B_\| \gg B_\perp$. Therefore, such changes in the polarization of $\mathbf{B}$ are unlikely to be observed by SCM.

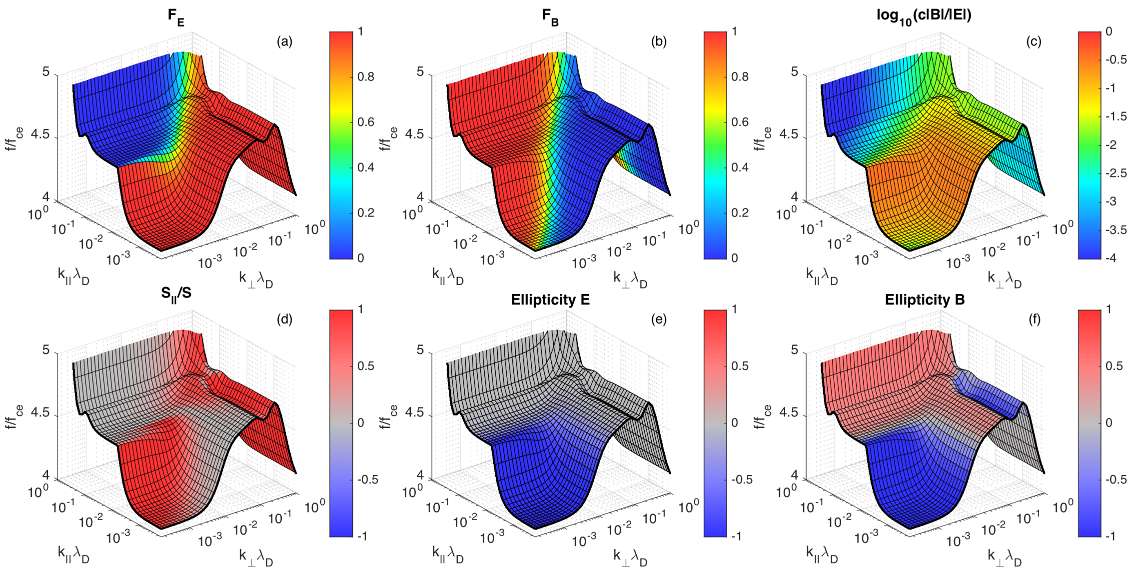

Figure A.1. Langmuir/Z-mode and upper hybrid dispersion surface. (a) F_E. (b) F_B. (c) $c|\mathbf{B}|/|\mathbf{E}|$. (d) $S_{\|}/S$. (e) Ellipticity of **E**. (f) Ellipticity of **B**. The dispersion surface is computed from hot and cold electron Maxwellian distributions with total density $n_e = 0.5\,\mathrm{cm}^{-3}$ and $B_0 = 50\,\mathrm{nT}$. For the cold population we use $n_{ec} = 0.95 n_e$ and $T_{ec} = 100\,\mathrm{eV}$ and for the hot population we use $n_{ec} = 0.05 n_e$ and $T_{ec} = 2\,\mathrm{keV}$. The wave numbers are normalized to the Debye length λ_D of the cold electron component.

(3) Although $c|\mathbf{B}|/|\mathbf{E}|$ is essentially unchanged as a function of $\mathbf{k}$, the values of $\mathbf{k}$ where $v_g = 0$ differs. Thus, assuming the observed waves have $v_g \approx 0$ the predicted $c|\mathbf{B}|/|\mathbf{E}|$ will differ from the single Maxwellian prediction, and depend on the electron temperatures.

Overall, these changes in the electromagnetic properties of UH waves when a two-component electron distribution is used instead of a single Maxwellian are very minor.

B: Upper hybrid and Bernstein waves near the upper hybrid frequency

For many wave events we observe large-amplitude UH waves and one of the Bernstein waves near f_{uh}. In these cases it can be difficult to determine which wave is the UH wave and which is the Bernstein wave, since the Bernstein wave can have an amplitude comparable to or larger than the UH wave. We investigate two wave events with UH and one of the Bernstein waves near f_{uh} and show that they have frequencies satisfying $v_g \approx 0$.

As the first example we show in more detail the wave event from Figures 7d–7f observed by MMS1 on 2015 December 22. For this event $f_{uh} \approx 8 f_{ce}$. Figure B.1a shows the waveform **E** in field-aligned coordinates over a short time interval. The waveform shows clear periodic beating due to two waves with distinct frequencies and similar amplitudes. The two spectral peaks associated with these waves are clearly seen in Figure B.1b. The spectral peaks lie just above and below $8 f_{ce}$, and away from $7.5 f_{ce}$ and $8.5 f_{ce}$. The frequency difference between the peaks is $\Delta f = 460$ Hz or $\Delta f / f_{ce} = 0.28$. The power is approximately minimal at $8 f_{ce}$.

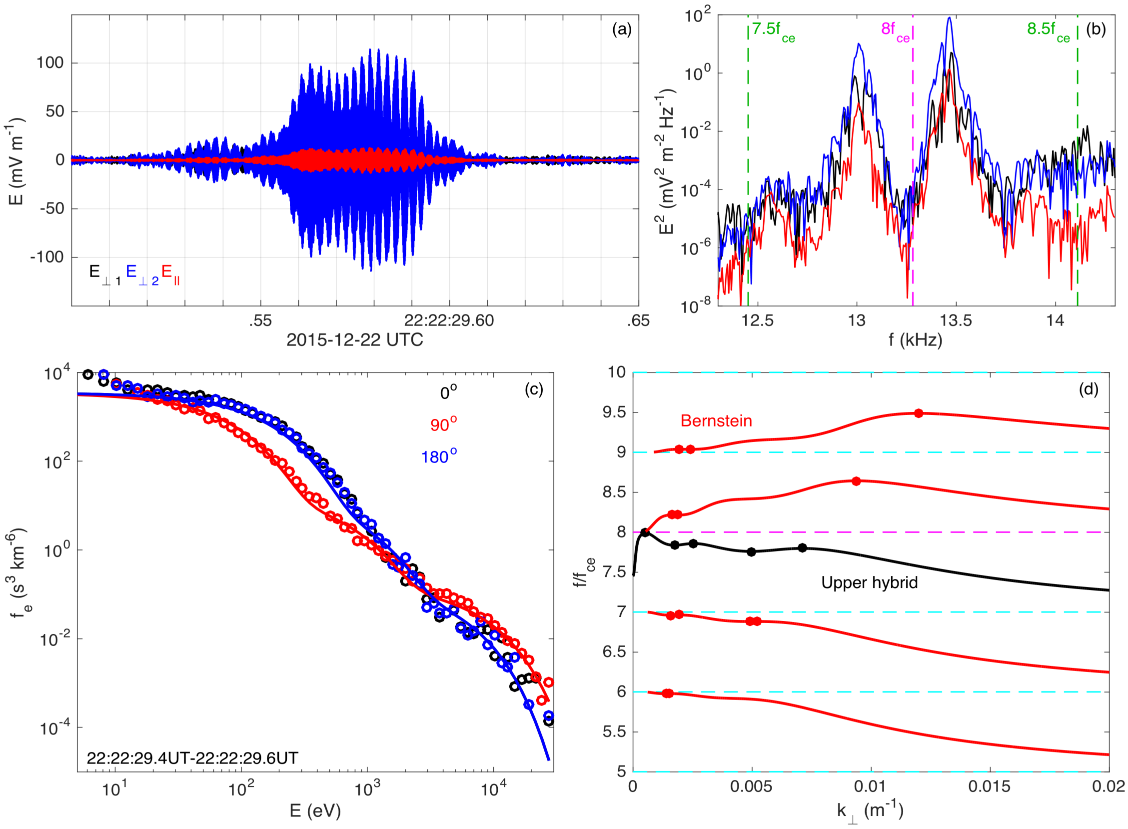

Figure B.1. UH waves observed by MMS1 on 2015 December 22. (a) **E** in field-aligned coordinates. (b) Power spectrum of **E** in field-aligned coordinates near $8 f_{ce}$ (magenta dashed line). The green dashed lines indicate $7.5 f_{ce}$ and $8.5 f_{ce}$. (c) Electron distribution at pitch angles $\theta = 0°, 90°$, and $180°$ when the waves are observed (circles) and a three bi-Maxwellian fit to the distribution (solid lines). (d) Dispersion relations of the UH wave (black line) and electron Bernstein waves (red lines) predicted from the fitted electron distribution in (c). The cyan dashed lines indicate $n f_e$ and the magenta dashed line indicates $f_{uh} = 8 f_{ce}$. The circles indicate points where $v_g = 0$.

Figure B.1c shows the electron distribution at pitch angles $\theta = 0°$, $90°$, and $180°$ at the time the UH waves are observed (to obtain the electron distribution we have averaged 0.2 s of data). Distinct hot and cold electron components are observed. The distribution is characterized by a parallel temperature anisotropy, $T_{\parallel} > T_{\perp}$, for energies $E \lesssim 1$ keV and a perpendicular temperature anisotropy, $T_{\parallel} < T_{\perp}$, for $E \gtrsim 1$ keV. Overplotted in Figure B.1c is our fit to the data using three bi-Maxwellian electron distributions. We have adjusted the densities to ensure that $f_{uh} = 8 f_{ce}$. Overall, we are able to well model all the features of the observed distribution.

We now use this fitted distribution and the local $B_0 = 59$ nT to compute the linear dispersion relations of the UH wave and the electron Bernstein waves near f_{uh}. The dispersion relations are shown in Figure B.1d along $k_{\perp}$. The UH dispersion relation starts at the Z-mode cutoff and peaks in frequency just below $f_{uh} = 8 f_{ce}$, i.e., it does not cross the UH resonance. For the UH mode there are 5 points with $v_g = 0$, due to the three bi-Maxwellian electron distributions used to compute the dispersion relation. Aside from the point with $f \approx f_{uh}$, these points correspond to $7.7 f_{ce} < f < 7.9 f_{ce}$, consistent with the lower observed spectral peak. The Bernstein mode between $8 f_{ce}$ and $9 f_{ce}$ approaches the UH mode, where the frequency of the UH mode peaks. For this Bernstein wave we observe three points where $v_g = 0$. The two points at lower $k_{\perp}$ correspond to $f \approx 8.2 f_{ce}$, consistent with the upper observed spectral peak. Similar variations in f are observed for the other Bernstein dispersion relations just above and below the UH mode, due to the non-Maxwellian electron distribution, although these fluctuations are less pronounced or are not observed far from f_{uh}. Based on these dispersion relations the spectral peak observed just above $8 f_{ce}$ in Figure B.1b corresponds to the Bernstein wave and the spectral peak just below $8 f_{ce}$ is the UH wave. If we assume that the observed waves have comparable $k_{\perp}$, Figure B.1d suggests that the waves would need to have relatively small $k_{\perp}$ to account for the observed frequency difference, i.e., $k_{\perp} \sim 2 \times 10^{-3}\,\mathrm{m}^{-1}$, or wavelength $\lambda_{\perp} \sim 3$ km. From this event, we conclude that both the UH wave and Bernstein waves near f_{uh} can reach large amplitudes. Finally, we note that if f_{uh} is slightly increased above $8 f_{ce}$ the UH mode would cross f_{uh} and have a dispersion relation similar to the Bernstein mode just above $8 f_{ce}$, while the UH mode shown in Figure B.1d would become the Bernstein wave just below f_{uh}. This is also a valid interpretation, but does not significantly modify the preceding discussion.

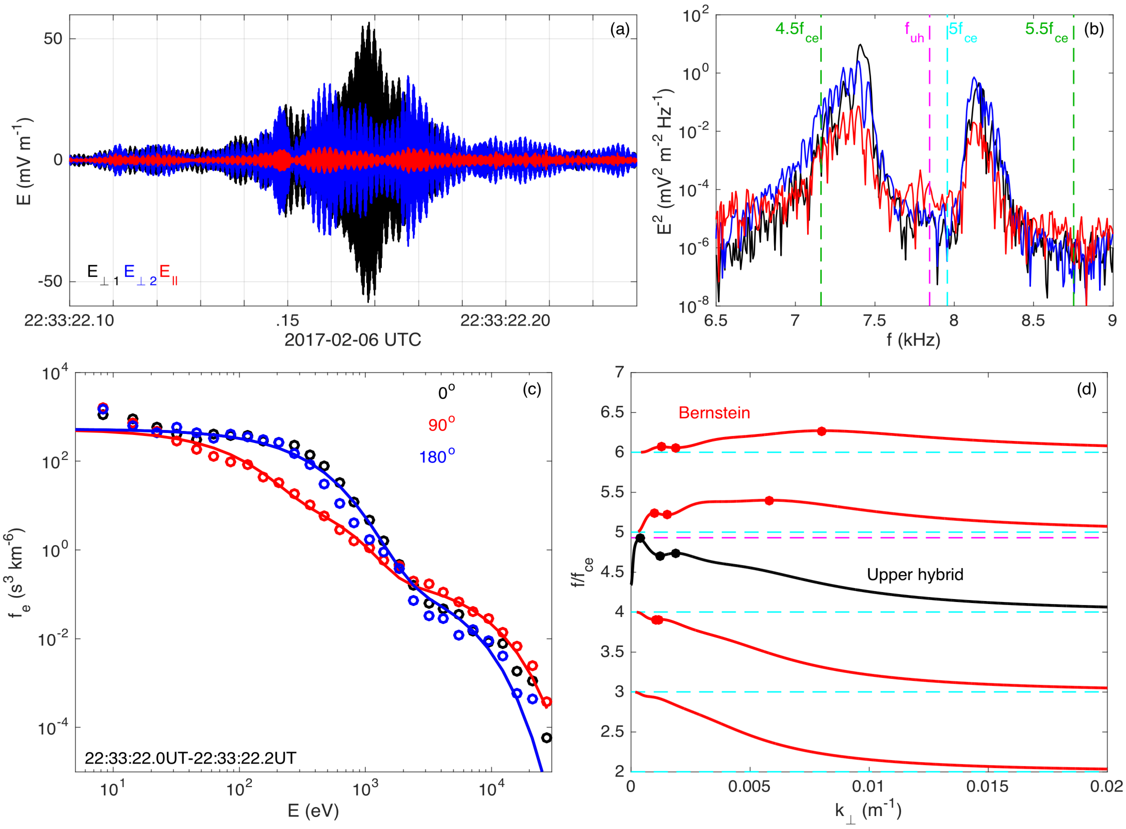

1113 **Figure B.2.** UH waves observed by MMS2 on 2017 February 06, presented in the same format as Figure
1114 B.1. In (b) the green dashed lines indicate $4.5f_{ce}$ and $5.5f_{ce}$, the cyan dashed line indicates $5f_{ce}$, and the
1115 magenta line indicates f_{uh}. In (d) the cyan dashed lines indicate nf_e and the magenta dashed line indicates
1116 f_{uh}.

As the second example, Figure B.2 shows a similar waveform for a slightly more strongly magnetized plasma. For this event f_{uh} is just below $5f_{ce}$. Like the previous example, periodic beating in the waveform and two distinct spectral peaks are observed (Figures B.2a and B.2b). The two spectral peaks occur above and below f_{uh} and $5f_{ce}$ and are separated by $\Delta f = 720\,\mathrm{Hz}$ or $\Delta f/f_{ce} = 0.45$. Thus, neither wave has peak power at f_{uh}. In this case the largest power is found for the spectral peak below f_{uh}. The observed electron distribution and fit using three bi-Maxwellians are shown in Figure B.2c. Distinct hot and cold electron components are observed. At low energies there is a strong parallel temperature anisotropy, while at high energies ($E \gtrsim 3\,\mathrm{keV}$) there is a perpendicular temperature anisotropy. Thus, the distribution is similar to the one observed in Figure B.1c. The predicted dispersion relations of the UH and Bernstein waves, shown in Figure B.2d, are similar to those found in Figure B.1d. The UH wave, beginning at the Z-mode cutoff, has a maximum frequency at $f \approx f_{uh}$, although UH waves are not observed at this frequency. Based on the observed power spectrum the lower spectral peak likely corresponds to the small local maximum and minimum near $k_\perp \sim 1.5 \times 10^{-3}\,\mathrm{m}^{-1}$ of the UH dispersion relation, where $v_g \approx 0$, and the frequency is below f_{uh} but above $4.5f_{ce}$. Similarly, the upper spectral peak likely corresponds to the Bernstein mode between $5f_{ce}$ and $6f_{ce}$, where there is a local maximum and minimum in f at similar $k_\perp$ to the UH waves. Based on the dispersion relation of the upper Bernstein wave f is between $5f_{ce}$ and $5.5f_{ce}$, consistent with observations. The predicted $\Delta f/f_{ce} = 0.5$ between the UH mode and the upper Bernstein mode is in good agreement with the observed $\Delta f/f_{ce} = 0.45$. Thus, based on the linear dispersion relations $k_\perp \sim 1.5 \times 10^{-3}\,\mathrm{m}^{-1}$ or $\lambda_\perp \sim 4\,\mathrm{km}$.

These two examples show that f_{pk} can occur both above and below f_{uh} and large-amplitude electron Bernstein waves can develop near f_{uh}. Therefore, in some cases the observed values of f_{pk} likely correspond to one of the Bernstein waves near f_{uh} rather than the UH wave. In both examples the hot electrons have sufficiently high density to modify the dispersion relation of the UH waves and the Bernstein waves near f_{uh}, such that there are multiple points with $v_g = 0$. The observed wave frequencies are consistent with points on the dispersion relation where $v_g = 0$. These examples show that in observations if is often quite difficult to distinguish between the UH mode and the Bernstein modes near f_{uh}. Using the observed frequency differences it is possible to estimate $k_\perp$ of the waves. For the estimated values of $k_\perp$ the effects of Doppler shift on the observed wave frequencies are negligible.

References

Anderson, R. R., T. E. Eastman, C. C. Harvey, M. M. Hoppe, B. T. Tsurutani, and J. Etcheto (1982), Plasma waves near the magnetopause, *J. Geophys. Res.*, *87*, 2087–2107, doi: 10.1029/JA087iA04p02087.

André, M. (1985), Dispersion surfaces, *J. Plasma. Phys.*, *33*, 1–19, doi: 10.1017/S0022377800002270.

Ashour-Abdalla, M., and C. F. Kennel (1978), Nonconvective and convective electron cyclotron harmonic instabilities, *J. Geophys. Res.*, *83*, 1531–1543, doi: 10.1029/JA083iA04p01531.

Bale, S. D., P. J. Kellogg, K. Goetz, and S. J. Monson (1998), Transverse z-mode waves in the terrestrial electron foreshock, *Geophys. Res. Lett.*, *25*, 9–12, doi: 10.1029/97GL03493.

Bernstein, I. B. (1958), Waves in a Plasma in a Magnetic Field, *Phys. Rev*, *109*, 10–21, doi:10.1103/PhysRev.109.10.

Boehm, M. H., C. W. Carlson, J. P. McFadden, J. H. Clemmons, R. E. Ergun, and F. S. Mozer (1994), Wave rectification in plasma sheaths surrounding electric field antennas, *J. Geophys. Res.*, *99*, 21,361, doi:10.1029/94JA01766.

Budden, K. G., and D. Jones (1987), Conversion of electrostatic upper hybrid emissions to electromagnetic O and X mode waves in the earth's magnetosphere, *Annales Geophysicae*, *5*, 21–28.

Burch, J. L., T. E. Moore, R. B. Torbert, and B. L. Giles (2016), Magnetospheric Multiscale Overview and Science Objectives, *Space Sci. Rev.*, *199*, 5–21, doi:10.1007/s11214-015-0164-9.

Cairns, I. H. (1987), Fundamental plasma emission involving ion sound waves, *J. Plasma Phys.*, *38*, 169, doi:10.1017/S0022377800012496.

Cairns, I. H. (1987), Second harmonic plasma emission involving ion sound waves, *J. Plasma Phys.*, *38*, 179–198.

Cairns, I. H., and D. B. Melrose (1985), A theory for the 2fp radiation upstream of the Earth's bow shock, *J. Geophys. Res.*, *90*, 6637, doi:10.1029/JA090iA07p06637.

Christiansen, P., P. Gough, G. Martelli, J.-J. Bloch, N. Cornilleau, J. Etcheto, R. Gendrin, D. Jones, C. Beghin, and P. Decreau (1978), Geos I - Identification of natural magnetospheric emissions, *Nature*, *272*, 682–686, doi:10.1038/272682a0.

Ellis, G. R. (1956), The z propagation hole in the ionosphere, *Journal of Atmospheric and Terrestrial Physics*, *8*, 43–54, doi:10.1016/0021-9169(56)90090-3.

Ergun, R. E., D. Larson, R. P. Lin, J. P. McFadden, C. W. Carlson, K. A. Anderson, L. Muschietti, M. McCarthy, G. K. Parks, H. Reme, J. M. Bosqued, C. D'Uston, T. R. Sanderson, K. P. Wenzel, M. Kaiser, R. P. Lepping, S. D. Bale, P. Kellogg, and J.-L. Bougeret (1998), Wind Spacecraft Observations of Solar Impulsive Electron Events Associated with Solar Type III Radio Bursts, *Astrophys. J.*, *503*, 435–445, doi: 10.1086/305954.

Ergun, R. E., D. M. Malaspina, I. H. Cairns, M. V. Goldman, D. L. Newman, P. A. Robinson, S. Eriksson, J. L. Bougeret, C. Briand, S. D. Bale, C. A. Cattell, P. J. Kellogg, and M. L. Kaiser (2008), Eigenmode structure in solar-wind Langmuir waves, *Phys. Rev. Lett.*, *101*, 051,101, doi:10.1103/PhysRevLett.101.051101.

Ergun, R. E., S. Tucker, J. Westfall, K. A. Goodrich, D. M. Malaspina, D. Summers, J. Wallace, M. Karlsson, J. Mack, N. Brennan, B. Pyke, P. Withnell, R. Torbert, J. Macri, D. Rau, I. Dors, J. Needell, P.-A. Lindqvist, G. Olsson, and C. M. Cully (2016), The Axial Double Probe and Fields Signal Processing for the MMS Mission, *Space Sci. Rev.*, *199*, 167–188, doi:10.1007/s11214-014-0115-x.

Etcheto, J., and M. Faucheux (1984), Detailed study of electron plasma waves upstream of the earth's bow shock, *J. Geophys. Res.*, *89*(A8), 6631–6653, doi: 10.1029/JA089iA08p06631.

Farrell, W. M., M. D. Desch, M. L. Kaiser, and K. Goetz (2002), The dominance of electron plasma waves near a reconnection X-line region, *Geophys. Res. Lett.*, *29*, 1902, doi: 10.1029/2002GL014662.

Farrell, W. M., M. D. Desch, K. W. Ogilvie, M. L. Kaiser, and K. Goetz (2003), The role of upper hybrid waves in magnetic reconnection, *Geophys. Res. Lett.*, *30*, 2259, doi: 10.1029/2003GL017549.

Farris, M. H., and C. T. Russell (1994), Determining the standoff distance of the bow shock: Mach number dependence and use of models, *J. Geophys. Res.*, *99*, 17,681–17,689, doi:10.1029/94JA01020.

Field, G. B. (1956), Radiation by plasma oscillations, *Astrophys. J.*, *124*, 555–570, doi: 10.1086/146261.

Filbert, P. C., and P. J. Kellogg (1979), Electrostatic noise at the plasma frequency beyond the Earth's bow shock, *Journal of Geophysical Research: Space Physics*, *84*, 1369–1381, doi:10.1029/JA084iA04p01369.

Fitzenreiter, R. J., J. D. Scudder, and A. J. Klimas (1990), Three-dimensional analytical model for the spatial variation of the foreshock electron distribution function: Systematics and comparisons with isee observations, *J. Geophys. Res.*, *95*(A4), 4155–4173, doi:10.1029/JA095iA04p04155.

Fuselier, S. A., D. A. Gurnett, and R. J. Fitzenreiter (1985), The downshift of electron plasma oscillations in the electron foreshock region, *J. Geophys.Res.*, *90*, 3935–3946, doi:10.1029/JA090iA05p03935.

Graham, D. B., and I. H. Cairns (2013a), Constraints on the formation and structure of Langmuir eigenmodes in the solar wind, *Phys. Rev. Lett.*, *111*, 121,101, doi:10.1103/PhysRevLett.111.121101.

Graham, D. B., and I. H. Cairns (2013b), Electrostatic decay of Langmuir/z-mode waves in type III solar radio bursts, *J. Geophys. Res.*, *118*, 3968, doi:10.1002/jgra.50402.

Graham, D. B., and I. H. Cairns (2014), Dynamical evidence for nonlinear Langmuir wave processes in type III solar radio bursts, *J. Geophys. Res.*, *119*, 2430–2457, doi:10.1002/2013JA019425.

Graham, D. B., I. H. Cairns, D. R. Prabhakar, R. E. Ergun, D. M. Malaspina, S. D. Bale, K. Goetz, and P. J. Kellogg (2012), Do Langmuir wave packets in the solar wind collapse?, *J. Geophys. Res.*, *117*, A09,107, doi:10.1029/2012JA018033.

Graham, D. B., I. H. Cairns, and D. M. Malaspina (2014), Harmonic waves and sheath rectification in type III solar radio bursts, *J. Geophys. Res.*, *119*, 723, doi:10.1002/2013JA019317.

Graham, D. B., A. Vaivads, Y. V. Khotyaintsev, and M. André (2016), Whistler emission in the separatrix regions of asymmetric reconnection, *J. Geophys. Res.*, *121*, 1934–1954, doi:10.1002/2015JA021239.

Graham, D. B., Y. V. Khotyaintsev, A. Vaivads, C. Norgren, M. André, J. M. Webster, J. L. Burch, P.-A. Lindqvist, R. E. Ergun, R. B. Torbert, W. R. Paterson, D. J. Gershman, B. L. Giles, W. Magnes, and C. T. Russell (2017), Instability of agyrotropic electron beams near the electron diffusion region, *Phys. Rev. Lett.*, *119*, 025,101, doi:10.1103/PhysRevLett.119.025101.

Gurnett, D. A. (1975), The earth as a radio source - The nonthermal continuum, *J. Geophys. Res.*, *80*, 2751–2763, doi:10.1029/JA080i019p02751.

Gurnett, D. A., and L. A. Reinleitner (1983), Electron acceleration by landau resonance with whistler mode wave packets, *Geophys. Res. Lett.*, *10*, 603–606, doi:10.1029/GL010i008p00603.

Gurnett, D. A., R. R. Anderson, B. T. Tsurutani, E. J. Smith, G. Paschmann, G. Haerendel, S. J. Bame, and C. T. Russell (1979), Plasma wave turbulence at the magnetopause - Observations from ISEE 1 and 2, *J. Geophys. Res.*, *84*, 7043–7058, doi:10.1029/JA084iA12p07043.

Jaynes, A. N., D. L. Turner, F. D. Wilder, A. Osmane, D. N. Baker, J. B. Blake, J. F. Fennell, I. J. Cohen, B. H. Mauk, G. D. Reeves, R. E. Ergun, B. L. Giles, D. J. Gershman, R. B. Torbert, and J. L. Burch (2016), Energetic electron acceleration observed by mms in the vicinity of an x-line crossing, *Geophys. Res. Lett*, *43*, 7356–7363, doi:10.1002/2016GL069206.

Jones, D. (1987), The magnetopause as a source of nonthermal continuum radiation, *Phys. Scr.*, *35*, 887–894, doi:10.1088/0031-8949/35/6/022.

Kellogg, P. J., K. Goetz, and S. J. Monson (2010), Harmonics of langmuir waves in the Earth's foreshock, *J. Geophys. Res.*, *115*, A06,107, doi:10.1029/2009JA014635.

Kellogg, P. J., K. Goetz, S. J. Monson, and A. Opitz (2013), Observations of transverse Z mode and parametric decay in the solar wind, *J. Geophys. Res.*, *118*, 4766, doi:10.1002/jgra.50443.

Khotyaintsev, Y., A. Vaivads, Y. Ogawa, B. Popielawska, M. André, S. Buchert, P. Décréau, B. Lavraud, and H. Rème (2004), Cluster observations of high-frequency waves in the exterior cusp, *Annales Geophysicae*, *22*, 2403–2411, doi:10.5194/angeo-22-2403-2004.

Kim, E.-H., I. H. Cairns, and P. A. Robinson (2007), Extraordinary-mode radiation produced by linear-mode conversion of Langmuir waves, *Phys. Rev. Lett.*, *99*, 015,003, doi:10.1103/PhysRevLett.99.015003.

Krauss-Varban, D. (1989), Beam instability of the Z mode in the solar wind, *J. Geophys. Res.*, *94*, 3527–3534, doi:10.1029/JA094iA04p03527.

Kurth, W., J. Craven, L. Frank, and D. Gurnett (1979), Intense electrostatic waves near the upper hybrid resonance frequency, *J. Geophys. Res.*, *84*(A8), 4145–4164, doi:10.1029/JA084iA08p04145.

Kurth, W. S. (1982), Detailed observations of the source of terrestrial narrowband electromagnetic radiation, *Geophys. Res. Lett.*, *9*(12), 1341–1344, doi:

10.1029/GL009i012p01341.

Kurth, W. S., L. A. Frank, D. A. Gurnett, B. G. Burek, and M. Ashour-Abdalla (1980), Observations of a free-energy source for intense electrostatic waves, *Geophys. Res. Lett.*, *7*, 293–296, doi:10.1029/GL007i005p00293.

Kurth, W. S., D. A. Gurnett, and R. R. Anderson (1981), Escaping nonthermal continuum radiation, *J. Geophys. Res.*, *86*, 5519–5531, doi:10.1029/JA086iA07p05519.

Layden, A., I. H. Cairns, B. Li, and P. A. Robinson (2013), Electrostatic decay in a weakly magnetized plasma, *Phys. Rev. Lett.*, *110*, 185,001, doi:10.1103/PhysRevLett.110.185001.

Le Contel, O., P. Leroy, A. Roux, C. Coillot, D. Alison, A. Bouabdellah, L. Mirioni, L. Meslier, A. Galic, M. C. Vassal, R. B. Torbert, J. Needell, D. Rau, I. Dors, R. E. Ergun, J. Westfall, D. Summers, J. Wallace, W. Magnes, A. Valavanoglou, G. Olsson, M. Chutter, J. Macri, S. Myers, S. Turco, J. Nolin, D. Bodet, K. Rowe, M. Tanguy, and B. de la Porte (2016), The Search-Coil Magnetometer for MMS, *Space Sci. Rev.*, *199*, 257–282, doi:10.1007/s11214-014-0096-9.

Lin, R. P., D. W. Potter, D. A. Gurnett, and F. L. Scarf (1981), Energetic electrons and plasma waves associated with a solar type III radio burst, *Astrophys. J.*, *251*, 364, doi:10.1086/159471.

Lindqvist, P.-A., G. Olsson, R. B. Torbert, B. King, M. Granoff, D. Rau, G. Needell, S. Turco, I. Dors, P. Beckman, J. Macri, C. Frost, J. Salwen, A. Eriksson, L. Åhlén, Y. V. Khotyaintsev, J. Porter, K. Lappalainen, R. E. Ergun, W. Wermeer, and S. Tucker (2016), The Spin-Plane Double Probe Electric Field Instrument for MMS, *Space Sci. Rev.*, *199*, 137–165, doi:10.1007/s11214-014-0116-9.

Malaspina, D. M., I. H. Cairns, and R. E. Ergun (2010), The 2f(p) radiation from localized Langmuir waves, *J. Geophys. Res.*, *115*, A01,101, doi:10.1029/2009JA014609.

Malaspina, D. M., I. H. Cairns, and R. E. Ergun (2011), Dependence of Langmuir wave polarization on electron beam speed in type III solar radio bursts, *Geophys. Res. Lett.*, *38*, L13,101, doi:10.1029/2011GL047642.

Malaspina, D. M., D. B. Graham, R. E. Ergun, and I. H. Cairns (2013), Langmuir wave harmonics due to driven nonlinear currents, *J. Geophys. Res.*, *118*, 6880, doi:10.1002/2013JA019309.

Melrose, D. B. (1981), A theory for the nonthermal radio continua in the terrestrial and Jovian magnetospheres, *J. Geophys. Res.*, *86*, 30–36, doi:10.1029/JA086iA01p00030.

Oya, H. (1971), Conversion of Electrostatic Plasma Waves into Electromagnetic Waves: Numerical Calculation of the Dispersion Relation for All Wavelengths, *Radio Science*, *6*, 1131–1141, doi:10.1029/RS006i012p01131.

Pollock, C., T. Moore, A. Jacques, J. Burch, U. Gliese, Y. Saito, T. Omoto, L. Avanov, A. Barrie, V. Coffey, J. Dorelli, D. Gershman, B. Giles, T. Rosnack, C. Salo, S. Yokota, M. Adrian, C. Aoustin, C. Auletti, S. Aung, V. Bigio, N. Cao, M. Chandler, D. Chornay, K. Christian, G. Clark, G. Collinson, T. Corris, A. De Los Santos, R. Devlin, T. Diaz, T. Dickerson, C. Dickson, A. Diekmann, F. Diggs, C. Duncan, A. Figueroa-Vinas, C. Firman, M. Freeman, N. Galassi, K. Garcia, G. Goodhart, D. Guererro, J. Hageman, J. Hanley, E. Hemminger, M. Holland, M. Hutchins, T. James, W. Jones, S. Kreisler, J. Kujawski, V. Lavu, J. Lobell, E. LeCompte, A. Lukemire, E. MacDonald, A. Mariano, T. Mukai, K. Narayanan, Q. Nguyan, M. Onizuka, W. Paterson, S. Persyn, B. Piepgrass, F. Cheney, A. Rager, T. Raghuram, A. Ramil, L. Reichenthal, H. Rodriguez, J. Rouzaud, A. Rucker, Y. Saito, M. Samara, J.-A. Sauvaud, D. Schuster, M. Shappirio, K. Shelton, D. Sher, D. Smith, K. Smith, S. Smith, D. Steinfeld, R. Szymkiewicz, K. Tanimoto, J. Taylor, C. Tucker, K. Tull, A. Uhl, J. Vloet, P. Walpole, S. Weidner, D. White, G. Winkert, P.-S. Yeh, and M. Zeuch (2016), Fast Plasma Investigation for Magnetospheric Multiscale, *Space Sci. Rev.*, *199*, 331–406, doi:10.1007/s11214-016-0245-4.

Reinleitner, L. A., D. A. Gurnett, and D. L. Gallagher (1982), Chorus-related electrostatic bursts in the earth's outer magnetosphere, *Nature*, *295*, 46–48, doi:10.1038/295046a0.

Reinleitner, L. A., D. A. Gurnett, and T. E. Eastman (1983), Electrostatic bursts generated by electrons in Landau resonance with whistler mode chorus, *J. Geophys. Res.*, *88*, 3079–3093, doi:10.1029/JA088iA04p03079.

Retinò, A., A. Vaivads, M. Andre, F. Sahraoui, Y. Khotyaintsev, J. S. Pickett, M. B. B. Cattaneo, M. F. Marcucci, M. Morooka, C. J. Owen, S. C. Buchert, and N. Cornilleau-Wehrlin (2006), Structure of the separatrix region close to a magnetic reconnection X-line: Cluster observations, *Geophys. Res. Lett.*, *33*, L06,101, doi:10.1029/2005GL024650.

Rönnmark, K. (1982), WHAMP – Waves in homogeneous, anisotropic, multicomponent plasmas, *technical report, Kiruna Geophys. Inst., Kiruna, Sweden*.

Russell, C. T., B. J. Anderson, W. Baumjohann, K. R. Bromund, D. Dearborn, D. Fischer, G. Le, H. K. Leinweber, D. Leneman, W. Magnes, J. D. Means, M. B. Moldwin, R. Nakamura, D. Pierce, F. Plaschke, K. M. Rowe, J. A. Slavin, R. J. Strangeway, R. Torbert, C. Hagen, I. Jernej, A. Valavanoglou, and I. Richter (2016), The magnetospheric multiscale magnetometers, *Space Sci. Rev.*, *199*, 189–256, doi:10.1007/s11214-014-0057-3.

Scarf, F. L., R. W. Fredricks, L. A. Frank, and M. Neugebauer (1971), Nonthermal electrons and high-frequency waves in the upstream solar wind, 1. observations, *J.Geophys. Res.*, *76*(22), 5162–5171, doi:10.1029/JA076i022p05162.

Schleyer, F., I. H. Cairns, and E.-H. Kim (2014), Linear mode conversion of Langmuir/z mode waves to radiation: Averaged energy conversion efficiencies, polarization, and applications to Earth's continuum radiation, *J. Geophys. Res.*, *119*, 3392–3410, doi:10.1002/2013JA019364.

Shue, J.-H., P. Song, C. T. Russell, J. T. Steinberg, J. K. Chao, G. Zastenker, O. L. Vaisberg, S. Kokubun, H. J. Singer, T. R. Detman, and H. Kawano (1998), Magnetopause location under extreme solar wind conditions, *J. Geophys. Res.*, *103*, 17,691, doi:10.1029/98JA01103.

Stix, T. H. (1962), *The Theory of Plasma Waves*, McGraw-Hill, New York.

Tataronis, J. A., and F. W. Crawford (1970), Cyclotron harmonic wave propagation and instabilities: I. Perpendicular propagation, *Journal of Plasma Physics*, *4*, 231–248, doi:10.1017/S0022377800004979.

Vaivads, A., Y. Khotyaintsev, M. André, A. Retino, S. C. Buchert, B. N. Rogers, P. Decreau, G. Paschmann, and T. D. Phan (2004), Structure of the magnetic reconnection diffusion region for four-spacecraft observations, *Phys. Rev. Lett.*, *93*, 105,001, doi:10.1103/PhysRevLett.93.105001.

Viberg, H., Y. V. Khotyaintsev, A. Vaivads, M. André, and J. S. Pickett (2013), Mapping HF waves in the reconnection diffusion region, *Geophys. Res. Lett.*, *40*, 1032, doi:10.1002/grl.50227.

Wilder, F. D., R. E. Ergun, K. A. Goodrich, M. V. Goldman, D. L. Newman, D. M. Malaspina, A. N. Jaynes, S. J. Schwartz, K. J. Trattner, J. L. Burch, M. R. Argall, R. B. Torbert, P.-A. Lindqvist, G. Marklund, O. Le Contel, L. Mirioni, Y. V. Khotyaintsev, R. J. Strangeway, C. T. Russell, C. J. Pollock, B. L. Giles, F. Plaschke, W. Magnes, S. Eriksson, J. E. Stawarz, A. P. Sturner, and J. C. Holmes (2016), Observations of whistler mode waves with nonlinear parallel electric fields near the dayside magnetic reconnection separatrix by the Magnetospheric Multiscale mission, *Geophys. Res. Lett.*, *43*, 5909–5917, doi:10.1002/2016GL069473.

Winglee, R. M., and G. A. Dulk (1986), The electron-cyclotron maser instability as a source of plasma radiation, *Astrophys. J.*, *307*, 808–819, doi:10.1086/164467.

Wong, H. K., J. D. Menietti, C. S. Lin, and J. L. Burch (1988), Generation of electron conical distributions by upper hybrid waves in the earth's polar region, *Journal of Geophysical Research: Space Physics*, *93*, 10,025–10,028, doi:10.1029/JA093iA09p10025.

Yin, L., M. Ashour-Abdalla, M. El-Alaoui, J. M. Bosqued, and J. L. Bourgeret (1998), Generation of electromagnetic f(pe) and 2f(pe) waves in the Earth's electron foreshock via linear mode conversion, *Geophys. Res. Lett.*, *25*, 2609, doi:10.1029/98GL01989.

Yoon, P. H., A. T. Weatherwax, T. J. Rosenberg, J. LaBelle, and S. G. Shepherd (1998), Propagation of medium frequency (1–4 mhz) auroral radio waves to the ground via the z-mode radio window, *Journal of Geophysical Research: Space Physics*, *103*(A12), 29,267–29,275, doi:10.1029/1998JA900032.

Yoon, P. H., R. Gaelzer, T. Umeda, Y. Omura, and H. Matsumoto (2003), Harmonic Langmuir waves. I. nonlinear dispersion relation, *Phys. Plasmas*, *10*, 364, doi: 10.1063/1.1537238.

Zakharov, V. E. (1972), Collapse of Langmuir waves, *Sov. Phys. JETP*, *35*, 908.